Prospects for Detecting C II Emission during the Epoch of Reionization

Silva, Marta; Santos, Mario G.; Cooray, Asantha; Gong, Yan

PROSPECTS FOR DETECTING C II EMISSION DURING THE EPOCH OF REIONIZATION

Marta Silva[1,2,3,5], Mario G. Santos[1,3,4], Asantha Cooray[2], and Yan Gong[2,6]
[1] CENTRA, Instituto Superior Técnico, Technical University of Lisbon, Lisboa 1049-001, Portugal
[2] Department of Physics & Astronomy, University of California, Irvine, CA 92697, USA
[3] Department of Physics & Astronomy, University of Western Cape, Cape Town 7535, South Africa
[4] SKA SA, The Park, Park Road, Cape Town 7405, South Africa
[5] Kapteyn Astronomical Institute, The University of Groningen, Landleven 12, 9747 AD Groningen, The Netherlands
[6] National Astronomical Observatories, Chinese Academy of Sciences, 20A Datun Road, Chaoyang District, Beijing 100012, China
Received 2014 October 17; accepted 2015 May 1; published 2015 June 18

ABSTRACT

We produce simulations of the atomic C II line emission in large sky fields in order to determine the current and future prospects for mapping this line during the high-redshift epoch of reionization. We calculate the C II line intensity, redshift evolution, and spatial fluctuations using observational relations between C II emission and the galaxy star formation rate over the frequency range 200–300 GHz. We estimate an averaged intensity of $I_{C II} = (4 \pm 2) \times 10^2$ Jy sr^{-1} in the redshift range $z \sim 5.3$–8.5. Observations of the C II emission in this frequency range will suffer contamination from emission lines at lower redshifts, in particular CO rotational lines. Using simulations, we estimated the CO contamination to be $I_{CO} \approx 10^3$ Jy sr^{-1} (originating from galaxies at $z < 2.5$). Using detailed simulations of the C II and CO emission across a range of redshifts, we generate maps as a function of angle and frequency, fully taking into account this resolution and light-cone effects. In order to reduce the foreground contamination, we find that we should mask galaxies below redshifts ~2.5 with a CO(J:2–1) to CO (J:6–5) line flux density higher than 5×10^{-22} W m^{-2} or an AB magnitude lower than $m_K = 22$. We estimate that the additional continuum contamination originating in emission from stars and in dust, free–free, free–bound, and two-photon emission in the interstellar medium is of the order of 10^5 Jy sr^{-1}, which is well above the expected C II signal. We also consider the possibility of cross-correlating foreground lines with galaxy surveys in order to probe the intensity of the foregrounds. Finally, we discuss the expected constraints from two experiments capable of measuring the expected C II power spectrum.

Key words: galaxies: high-redshift – galaxies: ISM – galaxies: luminosity function, mass function – large-scale structure of universe – quasars: emission lines

1. INTRODUCTION

The epoch of reionization (EoR) is a fundamental stage in the history of large-scale structure formation. The process of hydrogen ionization was fueled by radiation from the first galaxies that formed in overdense regions. Therefore, this process depends on a large set of astrophysical and cosmological parameters (Venkatesan 2000).

There are already several experiments in operation using low-frequency telescopes, such as the Murchison Widefield Arrays (Tingay et al. 2013), the Giant Metrewave Radio Telescope (Paciga et al. 2011), the Precision Array for Probing the Epoch of Reionization (Parsons et al. 2010), and the Low Frequency Array (Rottgering et al. 2006), aimed at constraining this epoch through the measurement of the 21 cm signal. Future experiments such as Phase II of HERA[7] and the Square Kilometre Array low-frequency instrument (SKA1-LOW; Mellema et al. 2013) should push this measurement to even higher redshifts.

One of the main challenges for probing the EoR with the 21 cm line is that observations will be contaminated by foregrounds several orders of magnitude higher than the signal (Shaver et al. 1999). Although the frequency smoothness of these foregrounds provides a way to remove them (Santos et al. 2005; Chapman et al. 2012), the combination with calibration errors and systematics complicates the foreground cleaning process.

Independent ways to measure this signal and to probe the reionization process are therefore required in order to ensure the validity of our measurements related to reionization.

In this work we analyze the use of C II intensity mapping both to probe the EoR during its final stages and to confirm and complement the 21 cm data. Although not resolving individual sources, the intensity mapping technique has the advantage of measuring all the emission in a given frequency band originating from a relatively large sky patch. This way, it is sensitive to radiation from faint sources and the diffuse intergalactic medium (IGM), which at these high redshifts cannot be detected with other methods, but whose contribution to the total signal is often important (Gong et al. 2012; Silva et al. 2013). Compared to other techniques, intensity mapping has the advantage of providing three-dimensional spatial information of the sources of emission that can be used to further understand the processes of structure formation. Intensity maps can also be used as cosmological probes since the fluctuations in the intensity of emission/absorption lines are correlated with the underlying dark matter density fluctuations (Carilli 2011). In particular, with C II, we can make maps of the sources of ionization, while the 21 cm signal will simply be sensitive to the IGM.

We show the potential of C II intensity mapping by simulating mock observational cones of C II emission and its foregrounds at frequencies from 200 to 300 GHz, taking into account the light-cone effects. This allows us to test possible ways to reduce the foregrounds without erasing the signal. The main foregrounds in C II intensity maps from the EoR will be

---

[7] http://reionization.org

contamination from other far-infrared (FIR) emission lines from lower redshifts, in particular emission from CO rotational transitions. CO emission from normal galaxies at $z > 1$ is poorly constrained by observations. Therefore, in order to properly estimate the intensity of these lines and the contamination power spectra relative to C II observations, we used two independent methods. First, we used the simulated galaxy catalog from the SAX-sky simulation, which uses a phenomenological model to calculate the luminosities of different CO transitions (Obreschkow et al. 2009a). We then confirmed our predictions using IR luminosity functions (LFs) and other observational data to estimate the relative intensities of the several CO transitions.

We find that CO contamination is dominated by bright sources, and so it can be efficiently reduced by masking the pixels where radiation from these sources is observed. In order to apply this procedure, we need a complementary experiment to measure CO emission from galaxies brighter than a given flux. This can be done with galaxy surveys targeting the CO emission, which would on its own be a powerful astrophysical probe on the conditions of the interstellar medium (ISM). Alternatively, the masking of the contaminant galaxies could be done with a CO tracer, easier to be observed, such as the star formation rate (SFR) or the relative magnitude in a given filter.

We also explore the possibility of cross-correlating C II and 21 cm maps in order to obtain maps of the EoR that are clean from foregrounds and systematics. This is possible since two lines emitted from the same redshift will be observed at different frequencies, and so they will be contaminated mainly by uncorrelated foregrounds (Gong et al. 2012).

This paper is organized as follows. In Section 2 we describe how to estimate the C II emission. In Section 3 we describe the C II foregrounds. In Sections 4 and 5 we describe how we used simulations to generate the signal and the foregrounds. In Section 6 we present the parameters of an experiment able to measure the C II signal and the CO signal in the 200–300 GHz band. In Section 7, we discuss how to remove the C II foregrounds. We estimate the cross correlation between the H I and C II lines in Section 8 and conclude with a discussion of the results obtained in Section 9.

2. CALCULATING C II EMISSION

C II emission originates in (i) the ISM, (ii) photodissociation regions (PDRs), (iii) ionized regions (H II regions), (iv) cold atomic gas, or (v) CO-dark molecular gas (regions in the boundary of molecular clouds with H_2 but without CO gas). Observations of the relative intensity of different emission lines have shown that the main source of C II emission is the dense PDRs located in the boundary of H II regions. PDRs are dense and warm regions of the ISM located between H II regions and molecular clouds. They contain mostly neutral gas, but due to their proximity to O and B stars or active galactic nuclei (AGNs), the physical and chemical properties of the gas are set by the strong far-ultraviolet (FUV) field. The strong FUV to X-ray radiation that penetrates the PDR is absorbed by dust grains that emit electrons heating the gas, or by atoms with an energy threshold for ionization below the Lyα limit such as carbon, oxygen, and nitrogen. The FUV also causes transitions from atomic to molecular hydrogen and from ionized carbon to carbon monoxide (Hollenbach & Tielens 1997).

C II photons are emitted in PDRs as a cooling mechanism, and so they are a consequence of preexisting heat. CO-dark clouds are envelopes of dense H_2 gas with densities too low for carbon to be converted to CO, but which can be identified by their C II emission. The contribution from CO-dark clouds to the total C II budget is not yet clear, but recent studies of our galaxy indicate that it can be high (up to ∼28%; Pineda et al. 2013) under certain astrophysical conditions, more characteristic of the low-redshift universe. Diffuse cold atomic gas can be characterized by its emission in the hydrogen 21 cm line and in the C II line. The intensity of emission in this gas phase will be proportional to the collisional rate, which depends on the gas density and temperature and therefore also on FUV strength.

The carbon ionization energy is only 11.3 eV, which is less than the 13.6 eV necessary to ionize hydrogen, so at first we could expect, as was done in Gong et al. (2012), that all the carbon in H II regions would be ionized. There would then be a high emission in the C II 157 μm line since its excitation potential is only of 91 K. Under this assumption, most of the C II emission would come from the highest-density locations inside H II regions. However, this is not supported by observations: several observational maps of the spatial distribution of C II emission in galaxies indicate that the C II emission mainly originates in PDRs and that H II regions contribute only a few percent of the total C II emission (Lebouteiller et al. 2012; Rigopoulou et al. 2014). There are studies that indicate a contribution from H II regions that can reach up to 30% of the total C II emission (Carral et al. 1994; Stacey et al. 1999; Aannestad & Emery 2003; Rigopoulou et al. 2013). However, these studies point out that most C II emission originates in the low-density H II regions. The simpler explanation for this unexpected result is that the carbon in the denser places in H II regions is highly shielded from radiation by hydrogen, and so almost all of the ionized carbon is located in low-density regions.

The *Herschel* telescope and the SOFIA observatory were used to observe typical tracers of PDRs, H II regions, and other galactic regions (Kaneda et al. 2013), and these observations showed that C II emission has a more complex spatial structure than most other infrared (IR) lines. In order to properly estimate the C II emission from a galaxy, it is necessary to observe it with high spatial resolution, which is not possible for most distant galaxies. Alternatively, we can use the intensity mapping technique to measure the integrated C II emission from many galaxies.

2.1. Theoretical Formulas to Estimate C II Emission

The intensity of C II emission is given theoretically (Gong et al. 2012) as

$$I_\nu = \frac{hc}{4\pi H(z)(1+z)^3} A_{ul}\, f_{C\,II}^{grd}\, n_{C\,II}(z)$$
$$\times \frac{g_u}{g_l} \exp\left(-T_{\star,ul}/T_{S,ul}\right)$$
$$\times \left[1 - \frac{\exp\left(T_{\star,ul}/T_{S,ul}\right) - 1}{\left(2\,h\nu^3/c^2 I_\nu\right)_{\nu_{ul}}}\right], \tag{1}$$

where $f_{C\,II}^{grd}$ is the fraction of C II ions at the ground level $^2P_{1/2}$, $n_{C\,II}$ is the number density of once ionized carbon atoms, $H(z)$ is the hubble parameter, T_S is the spin temperature, and $T_\star \equiv h\nu_{ul}/k_B$ (where ν_{ul} is the frequency of the transition).

The statistical weights are $g_u = 4$ and $g_l = 2$, and the Einstein spontaneous emission coefficient is $A_{ul} = 2.36 \times 10^{-6}$ s^{-1}.

As many of the parameters in Equation (1) are poorly known and cannot be directly obtained from observations, we use an alternative formula, based on the halo model, to obtain the intensity of a line emitted from several galaxies in a relatively large volume. For this we made the simplification of assuming that the average luminosity of each of these galaxies is only a function of the mass of the dark matter halo that contains it and at most its redshift. The average intensity of a line is then given by

$$\bar{I}(z) = \int_{M_{min}}^{M_{max}} dM \frac{dn}{dM} \frac{L(M,z)}{4\pi D_L^2} y(z) D_A^2 \qquad (2)$$

where dn/dM is the halo mass function (Sheth & Tormen 1999), M is the halo mass, $M_{min} = 10^8\, M_\odot$, $M_{max} = 10^{14}\, M_\odot$, D_L is the proper luminosity distance, D_A is the comoving angular diameter distance, and $y(z) = d\chi/d\nu$, where χ is the comoving distance and ν is the observed frequency. The relation between the C II luminosity ($L_{C II}$) and the halo mass is physically based on the dependence of $L_{C II}$ on the number density of C II atoms, which should be proportional to the halo mass.

2.2. Calculating C II Emission Using Observationally Based Relations

The C II luminosity of a galaxy can be estimated from other observable quantities as long as there is a reasonable correlation between the two. For large volumes, since we integrate over several galaxies, it is even more reliable to use these observational relations to estimate the overall luminosity from these regions. C II emission is powered by FUV radiation, and so there is a correlation between these two quantities that can be converted to a relation between C II and FIR luminosities given that in the star-forming galaxies (which will dominate the signal) there is a known correlation between the FUV and FIR fluxes. The C II luminosity of a galaxy also depends on other astrophysical properties of the galaxy such as its metallicity; however, the average ratio $R = \dfrac{L_{C II}}{L_{FIR}}$ shil for nearby, late-type galaxies and for $10^8\, L_\odot \leqslant L_{FIR} \leqslant 10^{10.5}\, L_\odot$ is approximately constant (Boselli et al. 2002) and is given by

$$L_{C II(M,z)}[L_\odot] = 0.003 \times L_{FIR}. \qquad (3)$$

This relation is also consistent with recent observations of high-redshift galaxies (Stacey et al. 2010) and with observations of ULIRGs ($L_{IR} > 10^{11.5}\, L_\odot$), where a ratio of $R = (0.8\text{--}4) \times 10^{-3}$ in the C II to FIR luminosities was found (Rigopoulou et al. 2014). In PDRs the same ratio is inversely proportional to the strength of the ambient radiation field G_0, since L_{FIR} is proportional to G_0 and $L_{C II}$ depends weakly on G_0 (Kaufman et al. 1999). Therefore, this ratio is likely to slightly increase to low-mass galaxies (up to $R \sim 0.01$) and to decrease to high-mass galaxies. The IR and the FIR luminosities are connected by the following relation:

$$L_{IR}(8\text{--}1000\ \mu m) = (1.89 \pm 0.26) L_{FIR}(40\text{--}120\ \mu m), \qquad (4)$$

obtained by Cardiel et al. (2003) using the *IRAS* Bright Galaxies Sample from Soifer et al. (1989).

The integrated IR luminosity, $L_{IR} = L(8\text{--}1000\ \mu m)$, is related to the galaxies' SFR (ψ) by the Kennicutt (1998) relation:

$$L_{IR}(M,z)[L_\odot] = 5.8 \times 10^9 \psi(M,z)[M_\odot\ yr^{-1}]. \qquad (5)$$

Using Equations (3)–(5), we obtained the following relation between C II luminosity and SFR:

$$\begin{aligned} L_{C II(M,z)}[L_\odot] &= 0.003 \times L_{FIR}[L_\odot] \\ &= 0.003 \times 0.53 \times L_{IR}[L_\odot] \\ &= 9.22 \times 10^6 \psi(M,z)[M_\odot\ yr^{-1}]. \end{aligned} \qquad (6)$$

The connection between C II luminosity and the SFR can be easily understood in the case of C II emission arising from warm PDRs, since in this case the FUV radiation ionizes the carbon in the outer layers of the photon-dominated molecular clumps, which, in its turn, emits C II with a luminosity proportional to the FUV flux, which is linked to the galaxy SFR (De Looze et al. 2011). In H II regions the amount of ionized carbon should increase with the size of the region, which is proportional to the stellar radiation UV intensity. However, given that not all carbon is necessarily ionized at the same time in H II regions and that the C II luminosity of these regions also depends on the astrophysical conditions of the gas, one expects a considerable dispersion in the relation between C II luminosity from H II regions and the SFR. Alternative relations between the C II luminosity and the SFR, obtained using different galaxy data sets and using an SFR estimated from the IR luminosity or from the Hα luminosity, can be found, for example, in Boselli et al. (2002), De Looze et al. (2011), or Sargsyan et al. (2012). All of the referred observational studies indicate that the ratio between C II and SFR is smaller for ultraluminous galaxies, although these galaxies account for no more than a few percent of the total emission, which justifies our use of a constant ratio.

The first five observations of star-forming galaxies at $z \simeq 6.5$ detected by the ALMA experiment were published (see, e.g., Wang et al. 2013). These galaxies have upper limits for the C II luminosity below what is predicted by Equation (6). However, their SFRs are above $10\, M_\odot\ yr^{-1}$, which puts them in the region where a C II deficit was already expected. Observations of typical star-forming galaxies at $z \sim 5\text{--}6$, recently obtained with ALMA, show C II luminosities versus FIR ratios clearly above the usual values at $z = 0$ (Capak et al. 2015). Also, for intensity calculations, according to our model, galaxies with SFRs above $10\, M_\odot\ yr^{-1}$ only represent around 20% of the total C II intensity, and so when fitting the C II luminosity versus SFR relation in observational data, we should take into account that less intense galaxies (which are too faint to be observed especially at high redshifts) have a large weight in the C II intensity and that they are more likely to have a more robust $L_{C II}$/SFR ratio.

In order to obtain upper and lower bounds to our C II intensity estimation, we decided to use four models for the $L_{C II}$ versus SFR relation, to which we will refer as m_1, m_2, m_3, and m_4. While Equation (6) corresponds to parameterization m_2, parameterization m_1 corresponds to the recent fit to high-redshift galaxies by De Looze et al. (2014), and parameterizations m_3 and m_4 correspond to fits to the galaxies in Figure 4.

Table 1
Parameters for the $L_{C\,II}$ vs. SFR Relation

Model	$a_{LC\,II}$	$b_{LC\,II}$
m_1	0.8475	7.2203
m_2	1.0000	6.9647
m_3	0.8727	6.7250
m_4	0.9231	6.5234

These models can all be parameterized as

$$\log 10\left(L_{C\,II}[L_\odot]\right) = a_{LC\,II} \times \log 10\left(\psi[M_\odot]\right) + b_{LC\,II}, \quad (7)$$

with the values for $a_{LC\,II}$ and $b_{LC\,II}$ presented in Table 1.

Here the C II intensity was estimated using Equation (2) with the C II luminosity given by Equation (7), converted into a C II luminosity versus halo mass relation. The conversion between SFR and halo mass was made using simulated galaxy catalogs post-processed by De Lucia & Blaizot (2007) and Guo et al. (2011) from the Millennium and Millennium II dark matter simulations (Springel et al. 2005; Boylan-Kolchin et al. 2009). We did not use an observationally based relation since such a relation is not available for low halo masses and high redshifts. The galaxy SFR from the simulated catalogs is on average related to the mass of the dark matter halo containing the galaxy by

$$\psi(M, z) = M_0 \times \left(\frac{M}{M_a}\right)^a \left(1 + \frac{M}{M_b}\right)^b, \quad (8)$$

where the values for the parameters M_0, M_a, M_b, a, and b are available in Table 2 for redshifts lower than 20. The evolution of the SFR with mass can be seen in the left panel of Figure 1 for redshifts 6 and 8.

The use of this formula results in the star formation rate density (SFRD) evolution shown in the right panel of Figure 1 assuming a dark matter halo mass range from $10^8 M_\odot$ to $10^{14} M_\odot$. The Millennium and Millennium II simulations only go until a redshift of 20. However, unless we want to consider unusual stars, the relation for $z = 20$ should be a good approximation for $z > 20$, if required.

2.3. Calculating C II Emission Using Gas Physics

The maximum possible upper value for the C II emission can be obtained assuming that all the carbon in the hot gas (typical H II regions) in a galaxy is ionized and therefore emitting in the C II line, such as was done in Gong et al. (2012). Here we do a similar calculation but with an improved parameterization of the metallicity in the galaxies' hot gas obtained using the Guo et al. (2011) galaxy catalog for low-mass halos and the De Lucia & Blaizot (2007) galaxy catalog for high halo masses. The resulting relation between halo mass and metallicity in the hot gas component is shown in Figure 2. By analyzing this figure, we found that the metallicity in the lower-mass halos of the De Lucia & Blaizot (2007) simulation is lower than the one found in the halos from the Guo et al. (2011) simulation, although these simulations used very similar prescriptions to determine the galaxies' metallicity. Since the Guo et al. (2011) simulation has a much higher mass resolution, we believe that their results are more reliable for the low-luminosity halos,

since the halos in the De Lucia & Blaizot (2007) galaxy catalog are only well resolved for masses above $3 \times 10^{10} M_\odot$.

The average relation between M_Z and halo mass M in the referred simulated galaxy catalogs can therefore be parameterized in the form

$$M_Z(M) = M_0\left(M/M_a\right)^a \left(1 + M/M_b\right)^b$$
$$\times \left(1 + M/M_c\right)^c \times \left(1 + M/M_d\right)^d, \quad (9)$$

where at the redshift range 5.0–8.5 these parameters take the values $M_0 = z - 1$, $M_a = 1.0 \times 10^8 M_\odot$, $M_b = 9.0 \times 10^9 M_\odot$, $M_c = 2.0 \times 10^{12} M_\odot$, $M_d = 2.0 \times 10^{13} M_\odot$, $a = 1.7$, $b = 1.0$, $c = -5.0$, and $d = 2.5$.

Assuming that all the carbon in the hot gas is ionized and that the carbon mass corresponds to a fraction of 21% of the total mass in metals (this is the same percentage of carbon found in the Sun), we obtain $M_{C\,II} = 0.21 M_Z$. In reality only a fraction of the carbon in H II regions is ionized, which can be easily included in these calculations. At large enough volumes the number density of C II atoms can be estimated from the halo mass using the formula

$$n_{C\,II}^{sim}(z) = \int_{M_{min}}^{M_{max}} dM \frac{dn}{dM} \frac{M_{C\,II}(M, z)}{m_c}, \quad (10)$$

where m_c is the atomic carbon mass.

We can obtain an upper value for the intensity of C II emission in H II regions by replacing in Equation (1) the C II number density obtained from Equation (10). We estimated the C II number density by assuming that H II regions have an electronic temperature of 10^4 K and an electronic density of 10^4 cm^{-3} (these values correspond to saturation emission values as obtained in Gong et al. 2012).

In Figure 3 we show the C II intensity estimated assuming several models for the C II emission. The average intensity of C II emission in the redshift range shown is between $\bar{I}_{C\,II} \approx 6 \times 10^2$ Jy sr^{-1} for model m_1 and $\bar{I}_{C\,II} \approx 9 \times 10^1$ Jy sr^{-1} for model m_4. The average C II intensity, obtained by averaging models m_1 to m_4, between $z \sim 5.5$ and $z \sim 8.5$ is $\bar{I}_{C\,II} \approx 4 \pm 2 \times 10^2$ Jy sr^{-1}.

In Figure 4, the C II luminosity as a function of the SFR for the different methods described is shown together with observational points of normal local galaxies from Malhotra et al. (2001) and with observational upper limits for high-redshift galaxies. The observed high-redshift galaxies, presented in this figure, have high SFRs, which indicates that they are very massive and rare or that they have extreme SFRs/mass ratios. In either case these galaxies have little effect on the overall C II intensity.

The C II luminosities from ionized regions, presented in Figure 4, were obtained by assuming that $L_{C\,II}$ is linearly proportional to the halo mass and by determining the constant of proportionality between the two by imposing that Equations (1) and (2) give the same result. The relation between halo mass and SFR was assumed to follow Equation (4).

3. C II FOREGROUNDS

The C II line emitted in the redshift range ≈ 8.51–5.35 is observed at frequencies 200–300 GHz. C II is an FIR line, and so C II intensity maps will be contaminated by other IR lines

Table 2
SFR Parameters Based on the Average Relations from the Simulated Galaxy Catalogs

| Redshift Range	M_0	M_a	M_b	a	b
0.00–00.50	$10^{-8.855}$	1.0×10^8	8.0×10^{11}	2.7	−4.0
0.00–02.75	$10^{-9.097+0.484 \times z}$	1.0×10^8	8.0×10^{11}	2.7	−4.0
2.75–03.25	3.3×10^{-8}	1.0×10^8	4.0×10^{11}	2.7	−3.4
3.50–04.50	1.5×10^{-7}	1.0×10^8	3.0×10^{11}	2.6	−3.1
4.50–05.50	9.0×10^{-7}	1.0×10^8	3.0×10^{11}	2.4	−2.3
5.50–06.50	3.6×10^{-6}	1.0×10^8	2.0×10^{11}	2.25	−2.3
6.50–07.50	6.6×10^{-6}	1.0×10^8	1.6×10^{11}	2.25	−2.3
7.50–09.00	1.0×10^{-5}	1.0×10^8	1.7×10^{11}	2.25	−2.4
9.00–11.00	3.7×10^{-5}	1.0×10^8	1.7×10^{11}	2.1	−2.2
11.00–13.00	5.0×10^{-5}	1.0×10^8	1.5×10^{11}	2.1	−2.2
13.00–20.00	$[5.0 + (z - 13.0)] \times 10^{-5}$	1.0×10^8	$[1.5 + (z - 13) \times 0.015] \times 10^{11}$	2.1	$-2.2 - (z - 13) \times 0.03$
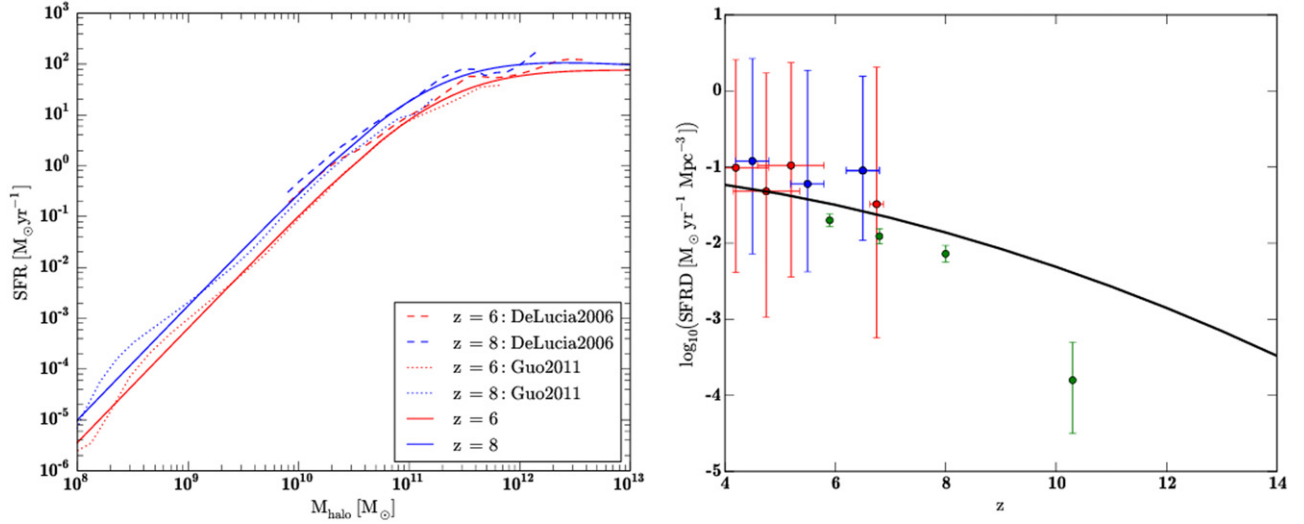
Figure 1. Left panel: star formation rate vs. halo mass for redshifts 6 (red upper lines) and 8 (blue upper lines). The dotted lines show the relations taken from the Guo et al. (2011) galaxy catalog for low halo masses; the dashed lines show the relation taken from the De Lucia & Blaizot (2007) galaxy catalog for high halo masses at the same redshifts. The solid lines show the parameterizations from Equation (8). Right panel: SFRD from the simulations (black solid line), obtained by integrating Equation (8) over the halo mass function. The green circles mark the SFRD corresponding to the UV luminosities corrected for dust extinction from Bouwens et al. (2012). The red and blue circles were obtained with measurements of gamma-ray bursts by Kistler et al. (2013) and Robertson & Ellis (2012), respectively.
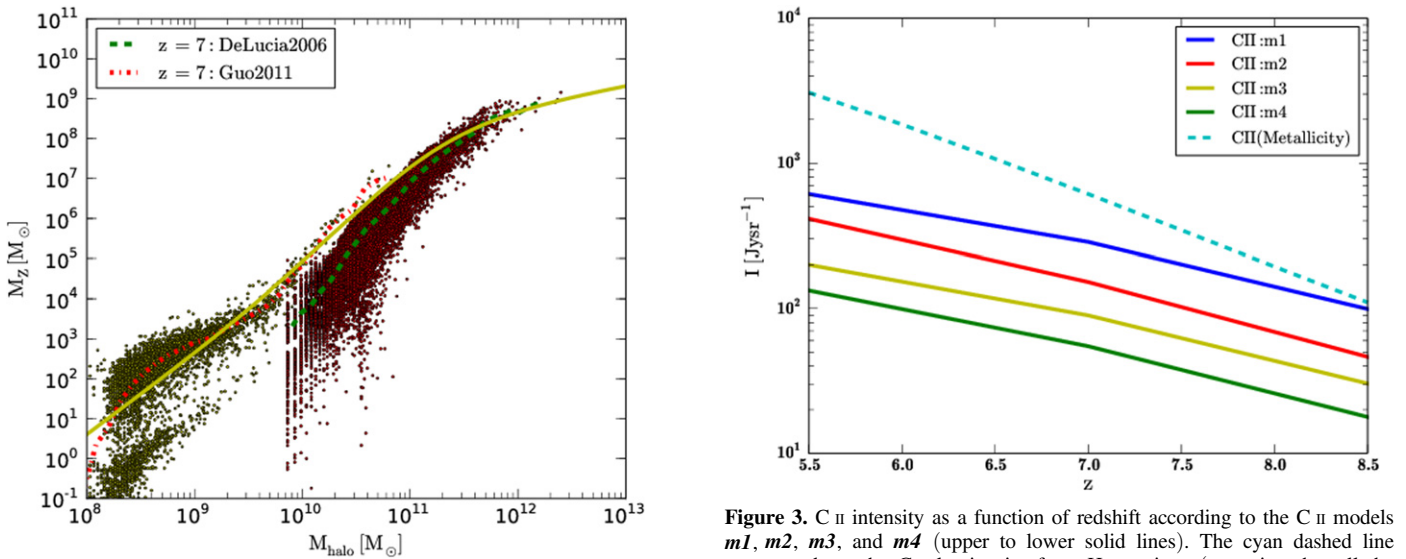

Figure 2. Mass in metals in the hot gas component M_Z as a function of the halo mass M at $z \approx 7$. The dot-dashed line shows the mean relation from the Guo et al. (2011) galaxy catalog, the dashed line shows the mean relation from the De Lucia & Blaizot (2007) galaxy catalog, and the solid line shows our fits to the mean values. The dots show the dark matter halos in the two catalogs.

Figure 3. C II intensity as a function of redshift according to the C II models *m1*, *m2*, *m3*, and *m4* (upper to lower solid lines). The cyan dashed line corresponds to the C II luminosity from H II regions (assuming that all the carbon is ionized).
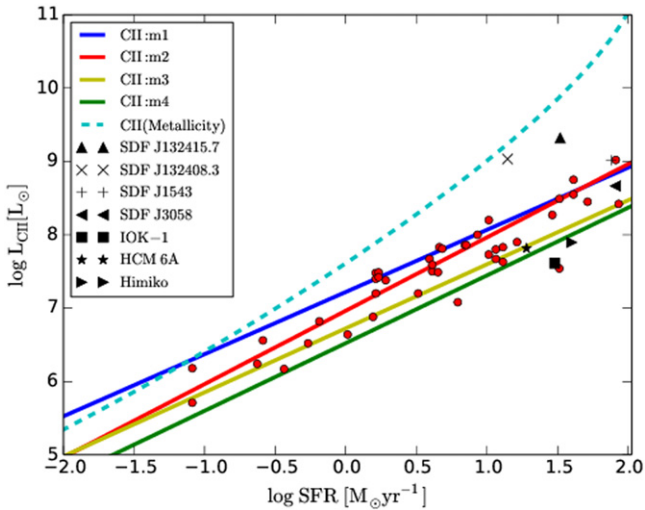
Figure 4. C II luminosity as a function of the SFR. The cyan dashed line corresponds to the C II luminosity from H II regions (assuming that all the carbon is ionized), and the solid lines correspond to the C II luminosity obtained from the SFR using relations *m1*, *m2*, *m3*, and *m4* (upper to lower lines). The red dots are local universe galaxies from the *ISO* Key Program (Malhotra et al. 2001), and the other symbols are upper limits from galaxies at $z > 6.5$ (taken from Kanekar et al. 2013; González-López et al. 2014; Ota et al. 2014).

and by IR continuum emission from galaxies and from the IGM. In this section we show estimations for the contamination from all of these extragalactic sources in the relevant observing frequency band. In addition, we also consider contamination due to emission from our Galaxy.

3.1. Contamination from Line Emission

The main contaminants in C II intensity maps will be emission lines from lower redshifts, namely, the [O I] 145 μm, the [N II] 122 μm, the [N II] 205 μm, and the CO rotation lines from transitions CO(2–1) and higher.

The [O I] 145 μm and the [N II] 205 μm lines are typical of PDRs, while the [N II] 122 μm line is typical of H II regions, and so the SFR can be used to roughly estimate their intensity of emission such as in the C II case (see Section 3.5). The CO lines are emitted from molecular gas, and their luminosities depend on several characteristics of the gas, and so we carefully estimate their intensity of emission in the next section.

3.2. CO Signal from Simulations

CO rotation lines will be the main contaminants in C II intensity maps observed at frequencies 200–300 GHz. Since the luminosities of the several relevant CO transitions are poorly constrained observationally, we estimate their intensities using the CO fluxes in the simulated galaxy catalog from Obreschkow et al. (2009a) and confirm our results with a CO intensity calculated using only observational relations, when available. The Obreschkow et al. (2009a) catalog is available for halo masses above $10^{10}\,M_\odot$ and provides astrophysical properties such as the CO fluxes for rotational transitions (1–0) to (10–9). The CO emission was estimated from the galaxies' molecular gas content and from the ISM temperature using physically based prescriptions and assuming thermal equilibrium.

Table 3
Emission Redshifts for the CO Rotational Transitions
in the Frequency Range 200–300 GHz

Transition (J)	ν_{CO}^J (GHz)	$Z(\nu_o \approx 300$ GHz)	$Z(\nu_o \approx 200$ GHz)
2–1	230.542	0	0.150
3–2	345.813	0.150	0.730
4–3	461.084	0.535	1.305
5–4	576.355	0.920	1.881
6–5	691.626	1.305	2.458
7–6	806.897	1.690	3.035
8–7	922.168	2.074	3.610
9–8	1037.439	2.458	4.186
10–9	1152.71	2.842	4.762

Each CO rotation line that is observed in the frequency range 200–300 GHz will come from the redshift range shown in Table 3. Note that for the CO(2–1), as is shown in Table 3, the minimum relevant redshift for this study is zero, which corresponds to the line rest frequency.

The CO intensity can be estimated from its luminosity as

$$\bar{I}_{CO}(\nu) = \sum_J \int_{M_{\min}}^{\infty} dM \frac{dn}{dM}(z, M) \frac{L_{CO}^J(z, M)}{4\pi D_L^2} y^J(z) D_A^2, \quad (11)$$

where the sum in J (angular momentum) is a sum over the luminosities of the different rotation lines from CO(2–1) to CO (6–5) and $z = \nu_{CO}^J/\nu_0 - 1$. We do not account for higher CO transitions since according to this CO model the CO contamination in C II intensity maps is highly dominated by the lower CO transitions. We also justify our choice by arguing that the contamination from transitions (7–6) and higher originates from high redshifts ($4.8 > z > 1.7$), and so the lower metallicity of these galaxies is likely to result in a considerably low CO emission.

Using the simulated fluxes, we parameterized the CO luminosity of galaxies as a function of halo mass for transitions CO(2–1) to CO(6–5) as

$$L_{CO}^J(M)[L_\odot] = L_0 \times M^{d0}$$
$$\times \left(1 + \frac{M}{M_{c1}}\right)^{d1} \left(1 + \frac{M}{M_{c2}}\right)^{d2}$$
$$\times \left(1 + \frac{M}{M_{c3}}\right)^{d3} \left(1 + \frac{M}{M_{c4}}\right)^{d4},$$
$$(12)$$

where the parameters for each transition can be found in Table 4. Note that these parameters were obtained for each transition by averaging the CO luminosity in the redshift range shown in Table 3.

Figure 5 shows the luminosity of the CO(2–1) transition as a function of halo mass, in the redshift range 0–0.15, obtained from the simulation.

Given that the minimum halo mass available in the Obreschkow et al. (2009a) galaxy catalog is not low enough for our study, we extrapolated the average CO luminosity to lower halo masses assuming that it is proportional to SFR at low masses. The CO luminosities were parameterized as a function of dark matter halo masses and not as a function of galaxy masses, and therefore for high halo masses they include

Table 4
CO Transition Luminosity Parameters

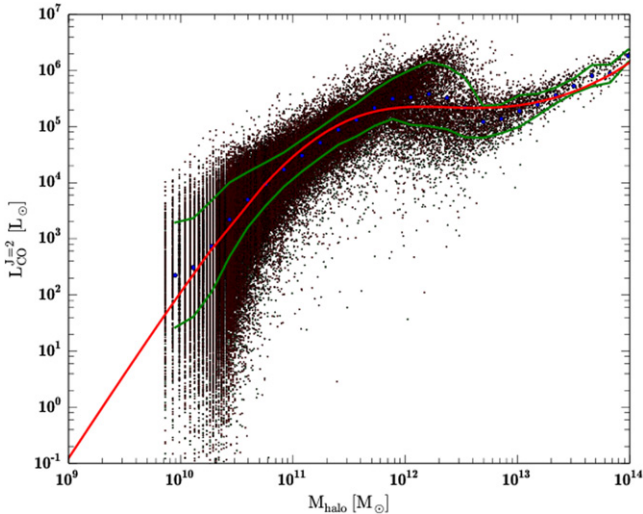| Trans	L_0	M_{c1}	M_{c2}	M_{c3}	M_{c4}	d0	d1	d2	d3	d4
2–1	4.70×10^{-29}	1.0×10^{11}	6.0×10^{11}	5.0×10^{12}	5.0×10^{14}	3.05	−2.0	−2.3	1.9	5.0
3–2	3.00×10^{-24}	6.0×10^{11}	5.0×10^{12}	4.0×10^{13}	0.0	2.6	−3.5	0.2	2.2	0.0
4–3	8.00×10^{-18}	9.0×10^{11}	5.0×10^{12}	3.0×10^{13}	0.0	2.05	−1.7	−1.8	2.3	0.0
5–4	3.50×10^{-18}	2.0×10^{12}	4.0×10^{12}	1.0×10^{13}	0.0	2.05	−2.0	−3.9	4.5	0.0
6–5	4.00×10^{-18}	9.0×10^{10}	6.0×10^{11}	0.0	0.0	2.0	1.5	−3.75	0.0	0.0

Figure 5. Luminosity of the CO(2–1) transition as a function of halo mass for the redshift band $z \sim$ 0–0.15. The black dots correspond to halos in the Obreschkow et al. (2009a) simulation. The blue dots show the mean of the scatter when binned in 30 logarithmic intervals in mass. The solid green lines show the $\pm 1\sigma$ relation. The red solid line corresponds to the parameterization given by Equation (12) with the parameters from Table 4.

the contribution from a main galaxy and several satellite galaxies. This parameterization could also have been made as a function of IR luminosity or SFR; however, galaxies powered by active galactic nuclei have relatively small IR luminosities, small SFRs, and high CO fluxes, and so this population would have to be taken into account separately.

The theoretical average power spectra of CO contamination presented in Figure 7 for transitions CO(2–1) to CO(6–5) indicate that the dominant contamination will be due to the low-J CO transitions. However, the ratios of different CO lines were obtained by assuming a simple model with a single gas component in local thermodynamic equilibrium. This does not necessarily have to represent well the molecular gas conditions in all types of galaxies. A more recent work described in Lagos et al. (2011) and Lagos et al. (2012) attempts to estimate the luminosity of the several CO transitions using an improved method to estimate the molecular gas content in galaxies. This is based on a somewhat more detailed model of the gas properties, as compared to Obreschkow et al. (2009a), used to estimate the relation between CO emission and molecular gas content. The main difference in the results obtained by these two authors is that the Lagos et al. (2012) model predicts a smaller molecular content in galaxies for $z > 2$ and higher ratios between the CO luminosities for higher transitions. These two corrections practically compensate themselves in terms of contamination in C II maps at the relevant frequencies for these studies, and so they should not have a significant effect in the validity of our predictions for intensity mapping. Even though

there are limitations to the CO luminosity calculation made by Obreschkow et al. (2009a), observationally only the CO(1–0) line is well constrained at small redshifts ($z \leqslant 1$), and in that case the CO LFs derived from the simulated galaxy catalog are compatible with observations. The few CO observations at $z > 1$ suggest a number density of CO emitters higher than what is predicted by the Obreschkow model (Daddi et al. 2010; Tacconi et al. 2010; Aravena et al. 2012); however, these observations are restricted to mainly the CO(2–1) transition from very high luminosity galaxies, while for the relevant observed frequency range the CO emission originates at $z < 1$, where the models are in better agreement.

3.3. CO Signal from Observations

An observational-only-based model to estimate the CO(1–0) luminosity is presented in Sargent et al. (2013), and so to support our conclusions, we used this completely independent model to estimate the CO contamination in C II maps. The Sargent model estimates CO emission from a recent IR LF at $z = 1$ presented in Sargent et al. (2012) and with the observational relations between IR and CO luminosities presented in Sargent et al. (2013). The LF is a useful way to put constraints on the overall luminosity of observed galaxies above a given luminosity limit characteristic of each survey. It corresponds to the number density of galaxies per luminosity interval as a function of luminosity. The LF is commonly plotted in units of number density per decade in luminosity ($\Phi[\text{Mpc}^{-3} \text{ dex}^{-1}]$), where dex accounts for the logarithmic variation of the luminosity for the bin used ($\log_{10} L_f - \log_{10} L_i$). The Sargent IR LF for $z \neq 1$ can be scaled with redshift using the factor $(1 + z)^{2.8}$ in the IR luminosity and scaling the number density as $\Phi \propto (1 + z)^{-2.4}$ for $z > 1.0$ (for lower redshifts the number density is fixed).

The CO luminosities can be obtained from the IR LF using

$$\log \left(\frac{L'_{\text{CO(J=1}\rightarrow 0)}}{\text{K km s}^{-1} \text{pc}^2} \right) = \alpha_1 + \beta_1 \log \left(\frac{L_{\text{IR}}}{L_\odot} \right) \quad (13)$$

where $(\alpha_1, \beta_1) = (0.18 \pm 0.02; 0.84 \pm 0.03)$ for normal galaxies and $(\alpha_1, \beta_1) = (-0.28^{+0.15}_{-0.09}; 0.84 \pm 0.03)$ for starbursts (Sargent et al. 2013). In Figure 6 the CO LF based on the Obreschkow et al. (2009b) model was obtained using a halo mass function and the CO luminosity parameterization from Equation (12). The two models shown in Figure 6 agree, taking into account the uncertainty in the relation between the IR luminosity and CO(1–0) luminosity used in the observational CO model (shown as shaded regions). The uncertainties in the Sargent CO LFs are even higher if we take into account the error bars in the IR LF, or the uncertainty in the passage from the CO(1–0) line to higher transitions.
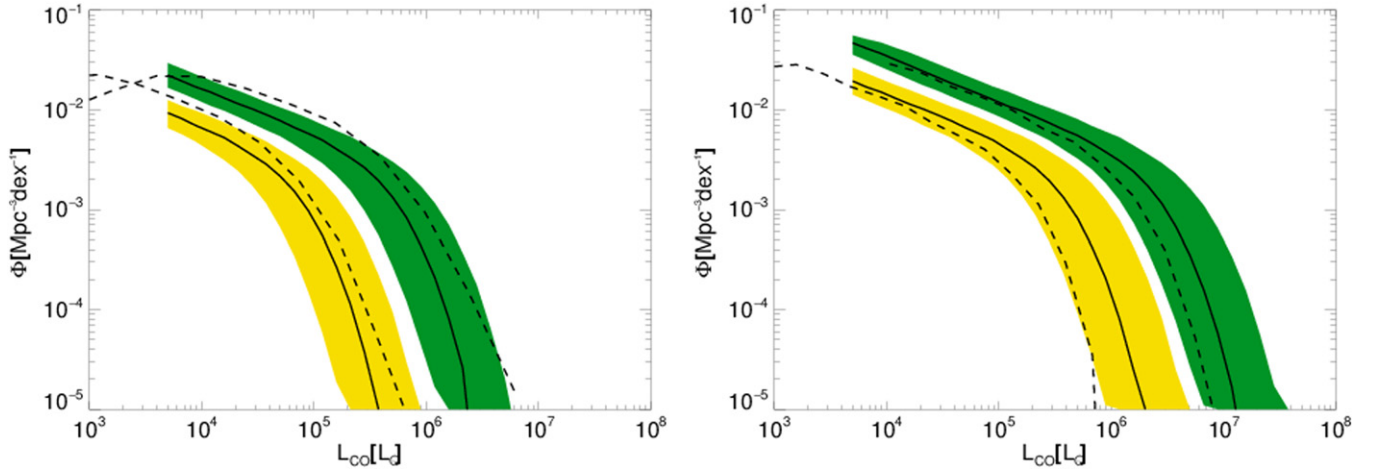
Figure 6. CO luminosity functions based on the Obreschkow et al. (2009a) CO model (dashed lines) and on the observational CO model (solid lines) at redshifts 0 (left panel) and 1 (right panel). The yellow and green regions show the uncertainty in the CO observational model due only to the uncertainty in the conversion factor between IR luminosity and CO(1–0) luminosity. The upper curves correspond to the transition CO(2–1), and the lower curves correspond to transition CO(1–0).

Ratios between the luminosities of the CO(1–0) line and higher CO transitions (in units proportional to the surface brightness L'_{CO} [K km s^{-1} pc^2]) for different types of galaxies are available in Carilli & Walter (2013). In order to obtain observational-only-based estimations for the LFs of the relevant CO transitions, we used the Sargent CO(1–0) model plus the Carilli & Walter (2013) observational ratios: $r_{21} = 0.85$, $r_{31} = 0.66$, $r_{41} = 0.46$, and $r_{51} = 0.39$, which are appropriate for submillimeter galaxies. Since there is no available observational relation between transitions CO(6–5) and CO(1–0), we assumed that $r_{61} = r_{51}$. For each transition the CO luminosity in $[L_\odot]$ can be obtained using

$$L_{CO} = 3 \times 10^{-11} \nu^3 L'_{CO}. \qquad (14)$$

We will from now on refer to the observational CO luminosities predicted using the Sargent CO(1–0) LF plus the Carilli et al. ratios for CO transitions as the observational CO model. The main differences between the two CO models lie in the conversion ratios between the luminosities of the several transitions given that the average ratios in the Obreschkow simulation are $r_{21} = 0.93$, $r_{31} = 0.70$, $r_{41} = 0.38$, $r_{51} = 0.12$, and $r_{61} = 0.02$ at a redshift close to zero and slightly increase for higher redshifts. The flux ratios in the Obreschkow simulation are appropriate for regular galaxies, while for starbursts and quasars the ratios between fluxes of high CO transitions are much higher. Recent observationally based ratios for different CO transitions as a function of redshift can be found in Daddi et al. (2015). This study suggests that the relative contribution from high CO transitions relevant for our study is even smaller than what is predicted by the two models discussed here. That is, it should be easier to remove CO contamination from observational maps. Given the lack of observational measurements of fluxes of high CO transitions in normal galaxies, with masses below $10^{12} M_\odot$, the ratios between different CO transitions and the LFs from these lines are poorly constrained, and this work can serve as motivation to plan an experiment especially designed to measure CO emission from several rotational transitions and their redshift evolution.

3.4. CO Signal: Intensity and Power Spectrum Estimates

We will now show theoretical estimates for the intensity and the power spectra of CO contamination using the LFs obtained with the two CO methods. The CO intensity can be obtained by integrating over the CO LF for the luminosity range available for each line. Following Gong et al. (2012), the CO intensity is given by

$$I_{CO}^J(\nu) = \int_{L_{max}^J}^{L_{min}^J} dL \frac{dn}{dL} \frac{L_{CO}^J}{4\pi D_L^2} y(z(\nu, J)) D_A^2, \qquad (15)$$

where $dn/dL = \Phi(L)$.

When calculating the power spectrum from a C II map contaminated by CO emission, the corresponding CO power spectrum will be rescaled from the original value at the CO emission redshift, both in amplitude and in terms of the wavelength. Following Gong et al. (2014), the contamination CO power spectra are given by

$$P_{obs}\left(k_\perp, k_\parallel\right) = \left[P_{CO}^{clus}\left(z_f, J, k_f\right) + P_{CO}^{shot}\left(z_f, J, k_f\right)\right]$$
$$\times \left(\left[\frac{\chi(z_s)}{\chi(z_f)}\right]^2 \left[\frac{y(z_s)}{y(z_f)}\right]\right), \qquad (16)$$

where the clustering power spectra are given by

$$P_{CO}^{clus}\left(z_f, J, k_f\right) = \bar{I}_f^2(z_f) b_f^2(z_f) P_{\delta\delta}\left(z_f, k_f\right). \qquad (17)$$

The indexes s and f indicate whether we are referring to, respectively, the source (C II) or the foreground (CO) redshifts, χ is the comoving distance, $|\mathbf{k}_f| = \left[(r_s/r_f)^2 k_\perp^2 + (y_s/y_f)^2 k_\parallel^2\right]^{1/2}$ is the three-dimensional k vector at the redshift of the foreground line, $P_{\delta\delta}$ is the matter power spectra, and b_{CO}^J is the bias between the CO($J \to J-1$) signal and dark matter.

The shot-noise power spectra due to the discrete nature of galaxies are given by

$$P_{CO}^{shot}(z, J) = \int_{M_{min}}^{M_{max}} dM \frac{dn}{dM} \left[\frac{L_{CO}^J(M, z)}{4\pi D_L^2} y(z, J) D_A^2\right]^2. \qquad (18)$$
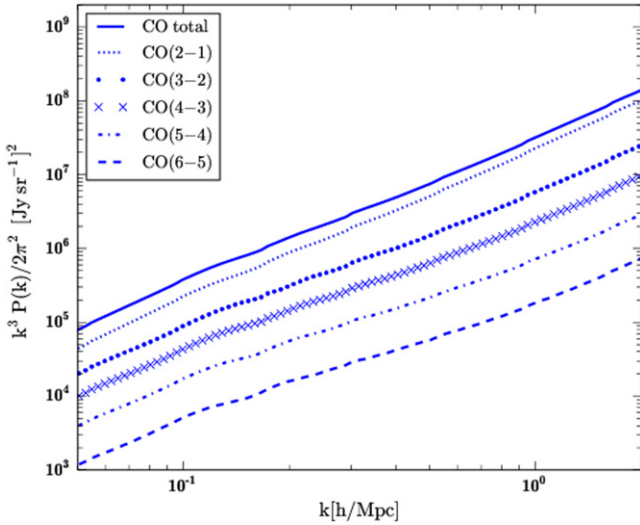
Figure 7. Power spectra of CO line emission made using the parameterization from Equation (12) in the frequency range 200–300 GHz projected to the redshift of the C II line. The top solid line shows the total CO power spectra, and the lower lines show the CO(2–1) to CO(6–5) transitions.
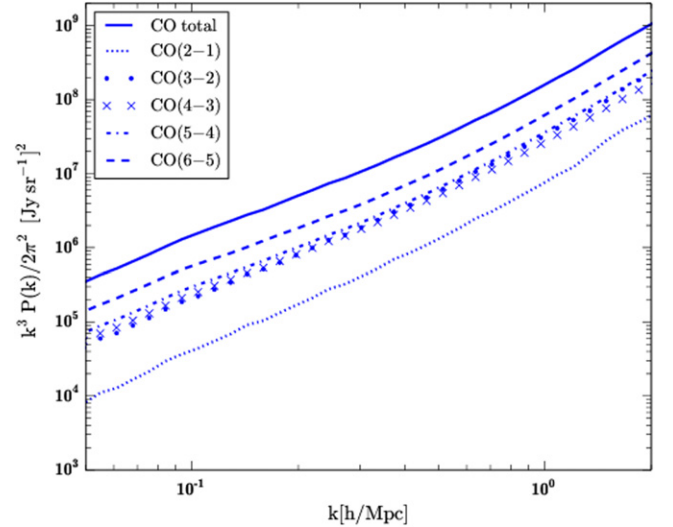

Figure 8. Power spectra of CO line emission made using the observational CO model in the frequency range 200–300 GHz projected to the redshift of the C II line. The top solid line shows the total CO power spectra, and the lower lines show the CO(2–1) to CO(6–5) transitions.

There are distortions in the observed power spectra in different directions due to redshift evolution of the signal. In theory these distortions could be used to differentiate between the signal and the foregrounds or to confirm whether the foregrounds where effectively removed since in that case there should be no distortions observed (besides the known redshift-space distortions). However, in practice this would require an experiment with an extremely high resolution, and so in this study we will only consider the spherical average power spectra. The foreground lines will contaminate the spherical average C II power spectra at $|\boldsymbol{k}_s| = \left[k_\parallel^2 + k_\perp^2\right]^{1/2}$.

Since we assume that there is a correlation between CO luminosity and dark matter halo mass, the bias between the overall CO emission and the underlying dark matter density field can be estimated from the halo bias $(b(z, M))$ as

$$b_{CO}^J = \frac{\int_{M_{min}}^{M_{max}} dM \frac{dn}{dM} L_{CO}^J(M, z) b(z, M)}{\int_{M_{min}}^{M_{max}} dM \frac{dn}{dM} L_{CO}^J(M, z)} \qquad (19)$$

where $M_{min} = M(L_{min}^J)$, $M_{max} = M(L_{max}^J)$, and $L_{CO}^J(M, z) \propto M^{\alpha_{CO}}$. The correct value for α_{CO} changes with the galaxy mass; assuming the values from the galaxies in the Obreschkow simulation, we have $\alpha_{CO} = 1.5 \pm 0.5$ for halos with $M < 10^{12} M_\odot$ and $\alpha_{CO} < 1$ for higher-mass halos. For the observationally based CO contamination power spectra we assume $\alpha_{CO} = 1$ in our calculations. The estimated contamination power spectra of CO emission in C II maps observed in the frequency range 200–300 GHz are shown in Figures 7 and 8 for the Obreschkow CO model and the observational CO model, respectively.

3.5. Contamination from Atomic Emission Lines

The [O I] 145 μm, [N II] 121.9 μm, and [N II] 205.2 μm atomic emission lines are emitted from PDRs or from H II regions, and so the luminosity of these lines is powered by

Table 5
Average Intensity of Several Emission Lines in the Observed Frequency Range 200–300 GHz in Units of [Jy sr^{-1}]

Line	[x]/[FIR]	z (200 GHz)	z (300 GHz)	Intensity
[O I] 145 μm	0.05%	9.3	5.9	5.1
[N II] 122 μm	0.01%	11.3	7.2	5.5
[N II] 205 μm	0.03%	6.3	3.9	58

stellar emission. Therefore, it is expected to be correlated with the galaxies' SFRs. The luminosity of these lines depends highly on the galaxies' gas density and FUV flux (Kaufman et al. 1999). However, for a large number of galaxies, their luminosity densities scale with the FIR luminosity. We therefore used the observational ratios, presented in Table 5 (taken from Brauher et al. 2008; Ferkinhoff et al. 2011; Graciá-Carpio et al. 2011; Zhao et al. 2013), to estimate the line luminosities ([x]/[FIR] stands for the average fraction of FIR emission of each line). The luminosity of these lines as a function of halo mass was then obtained using Equations (4), (5), and (8). The intensity of each line in the relevant range of 200–300 GHz, estimated using Equation (2), is shown in Table 5.

The average contamination from these lines is considerably below the C II intensity.

3.6. Contamination from Continuum Emission

The contamination from continuum emission can be estimated from the SFR and gas properties. The origins for the continuum emission considered here include stellar continuum emission that escapes the galaxy, stellar emission reprocessed by the dust in the galaxy, free–free and free–bound continuum emission caused by interactions between free electrons and ions in the galaxies, and two-photon emission originating during recombinations. Since continuum radiation (with the exception of some bands in stellar continuum radiation) observed in the frequency range 200–300 GHz will be emitted in the IR band, it will not be absorbed by any of the

Table 6
Intensity of Continuum Emission Observed at Frequencies
of 300 and 200 GHz in Units of (Jy sr^{-1})

Source of Emission	I (300 GHz)	I (200 GHz)
Dust	2.2×10^{-5}	1.8×10^{-7}
Stellar	4.1×10^{-3}	8.5×10^{-1}
Free–free+free–bound	2.4×10^{-12}	1.6×10^{-12}
Two-photon	3.4×10^{-12}	2.8×10^{-12}

main hydrogen lines or by dust, and so we can assume that this radiation is not affected during its path toward us.

The intensity of contamination from all of the referred continuum sources of IR emission is shown in Table 6, and the detailed calculations are presented in the Appendix.

It is also expected that there is some contamination from the Milky Way that can be estimated from temperature maps of our Galaxy for the relevant frequencies. Using temperature maps from Planck at frequencies 143, 217, and 353 GHz, we estimated that unless we were in the center of the Milky Way, where the brightness temperature can reach 0.2–0.3 K, the average brightness temperature is well below 0.1 K, which corresponds to an observed intensity of 2.44×10^{-32}–1.18×10^{-32} Jy sr^{-1} for 200 and 300 GHz, respectively.

The intensities in Table 6 show that the continuum contamination is below the C II signal, and so in principle it is not necessary to remove this contamination from observational C II intensity maps.

4. SIMULATIONS OF THE OBSERVED SIGNAL

The C II mock observational cone was made using the following steps.

1. A dark matter density field with a size of $L_{\rm box} = 634\ h^{-1}$ Mpc and a number of cells of $N_{\rm box}^3 = 1800^3$ was generated using the Simfast21 code (Santos et al. 2010; Silva et al. 2013).
2. The same code was used to generate dark matter halo catalogs from the previously generated density field using the excursion set formalism and by sampling the halos directly from the density field. These catalogs were made for redshifts 5.3–8.5 with a redshift step of 0.1 and a halo mass range of $10^8\ M_{\odot}$–$10^{15}\ M_{\odot}$. At this point the halo properties contained in the catalogs included only the halo mass and its position in a three-dimensional box with the size and resolution of the density field.
3. We randomly assigned astrophysical properties, such as SFR, from the De Lucia & Blaizot (2007) galaxy catalog, to the generated halos according only to the halo mass and redshift.
4. We added C II luminosities to the halo properties using the halo SFR versus C II luminosity relations shown in Section 2.1, which resulted in four C II luminosity values for each halo, one for each of the m_1, m_2, m_3, and m_4 models.
5. In order to build the observational cones, we made a box with 50 by 256^2 cells that covers the frequency range 200–300 GHz and the $1.3° \times 1.3°$ field of view with steps of, respectively, $df_{\rm o} = 2$ GHz and $d_{\rm ang} = 8 \times 10^{-3}$ deg. The angular coordinates correspond to positions in R.A. and decl., where the center of the box (the cone rotation axis) is at R.A. $= 0$ and decl. $= 0$.

6. We filled the box with the halos by assuming that the halo z position corresponds to its position in the direction of the line of sight and that moving in this direction is equivalent to moving in redshift. Since the size of the halo catalogs in the z direction is smaller than the comoving distance from redshift 5.3 to 8.5, we piled the catalogs in order to cover the entire needed distance range, but we rotated the upper catalogs in order to not repeat structures in the line-of-sight direction. The initial position of the halos was assumed to be at the comoving distance at which emitted C II photons are observed at a frequency of 300 GHz (d_{f300}). The position (x_i, y_i, z_i) of the halos was assumed to be at a distance $(d_x = x_i \times d_r - L_{\rm box}/2, \quad d_y = y_i \times d_r - L_{\rm box}/2,$ $\mathrm{dist}_Z = d_{f300} + z_i \times d_r)$, where $d_r = L_{\rm box}/N_{\rm box}$, which corresponds to a comoving distance $\mathrm{dist}_c = (d_x^2 + d_y^2 + d_z^2)^{1/2}$ and to an angular position in R.A. and decl. of, respectively,

$$\text{R.A.} = \arctan\left(\frac{d_{\rm x}}{d_{\rm com}}\right), \tag{20}$$

and

$$\text{decl.} = \arctan\left(\frac{d_{\rm y}}{d_{\rm com}}\right). \tag{21}$$

Each comoving position was converted first to a redshift and then to an observed frequency using $\nu_{\rm obs} = \nu_{\rm C\,II}/(1 + z)$. The halos were then distributed in the cone according to their angular position and observed frequency. For each halo catalog at a redshift z we only used the halos with a redshift lower than $z + dz$.

7. In each cell of the mock observing cone, the intensity was assumed to be given by a sum over the contribution from each galaxy as

$$I_{\rm C\,II} = \sum_i \frac{1}{df_{\rm o}} \frac{L_{\rm C\,II}(M, z)}{4\pi D_{\rm L}^2}. \tag{22}$$

5. SIMULATIONS OF THE CO FOREGROUND CONTAMINATION

The CO mock observational cones were made using the following steps.

1. A dark matter density field with a size of $L_{\rm halos}^3 = 296^3\ h^{-3}$ Mpc^3 and a number of cells of $N_{\rm halos} = 1200^3$ was generated using the Simfast21 code.
2. The same code was used to generate dark matter halo catalogs from the previously generated density field using the excursion set formalism and by sampling the halos directly from the density field. These catalogs were made for redshifts 0 to 2.5 with a redshift step of 0.1 and a halo mass range of $10^8\ M_{\odot}$–$10^{15}\ M_{\odot}$. The halo properties contained in the catalogs include only the halo mass and position in a three-dimensional box with the size and resolution of the density field.
3. We randomly assigned astrophysical properties, such as SFR, CO fluxes, and visual absolute magnitudes, from the De Lucia & Blaizot (2007) and the Obreschkow et al. (2009a) simulated galaxy catalogs to the halos (e.g., we
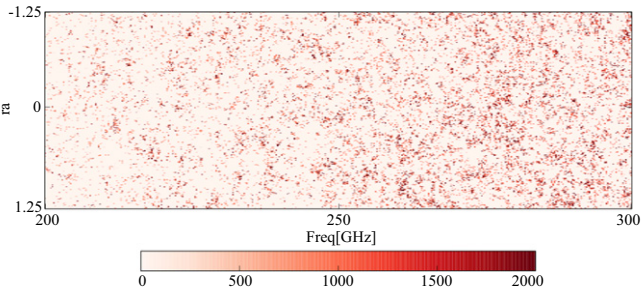
Figure 9. Slice of a C II mock observing cone with 2.5 square degrees for frequencies 200–300 GHz.

Table 7
Intensity of C II Emission from Galaxies as a Function of Redshift Calculated Using the SFR

$z_{C\,II}$	$\bar{I}_{C\,II}$	$I_{C\,II}^{max}$	$I_{C\,II}^{min}$	I_{CO}
8.5	47.0×10^1	9.50×10^1	1.80×10^1	1.05×10^3
7.5	1.00×10^2	2.00×10^2	3.70×10^1	1.25×10^3
6.5	1.90×10^2	3.50×10^2	7.50×10^2	1.12×10^3
5.5	3.36×10^2	6.00×10^2	1.33×10^2	1.06×10^3

Note. The medium, maximum, and minimum values of the C II intensity correspond to the $L_{C\,II}$ vs. SFR parameterizations m_2, m_1, and m_4, respectively. Also shown are the CO intensities estimated using the Obreschkow CO model. The intensities have units of (Jy sr^{-1}).

Table 8
Parameters for a C II Experiment

Instrument	C II-Stage I	C II-Stage II
Dish size (m)	10	10
Survey area A_s (arcmin^2)	78×0.5	600×600
Instantaneous FOV (arcmin^2)	13.6×0.5	25.6×0.4
Frequency range (GHz)	200–300	200–300
Frequency resolution (GHz)	2	0.4
Number of spectrometers	32	64
Total number of bolometers	1600	16000
On-sky integration time (hr)	1000	2000
NEFD[a] on sky (mJy $\sqrt{sec}$)	65	5

Note.
[a]Noise equivalent flux density (NEFD).

allowed some randomness in the astrophysical properties for halos with the same mass and redshift, using distributions from the SAX simulation).

4. We calculated the CO luminosity for each halo from its CO flux.

5. We repeated steps 5 and 6 of the C II signal generation assuming that the position $z = 0$ of the halos corresponded to a comoving distance of zero and that the redshift could be converted to an observed frequency using $\nu_{obs} = \nu_{CO}^J/(1 + z)$.

6. For each CO transition we built mock observing cones with intensities estimated as in the C II case, and then we added the cones to obtain the total CO intensity.

7. In order to simulate the effect of the masking technique, we made a mock observing cone with only the galaxies with CO fluxes above a given threshold. The pixels with at least one galaxy correspond to pixels that should be masked in order to decrease the CO contamination in C II observational maps, and so we put to zero the corresponding pixels in the initial CO box and in the C II box. We also used the same technique with a limit in magnitudes in the AB system K filter (m_K) instead of a limit in CO flux.

A slice of a mock observational C II cone is shown in Figure 9. This figure shows that C II emission is not randomly distributed but that it follows the underlying density fluctuations.

One of the advantages of simulating mock observational cones is that we can directly add the signal and its contaminants to obtain a more realistic version of an observational intensity map. This is useful because it gives us better predictions of what an observational experiment will actually measure and how to relate the observed signal to the intrinsic signal, which is where the scientific information really lies. The analysis of the information contained in these cones is mainly made using the power spectra of the target emission line, and so we used slices in frequency (these slices correspond to the signal emission around a given redshift) from these cones to construct intensity maps in Cartesian coordinates, from which we calculated the signal power spectra. With this method we directly mapped the contaminants' intensity spatial fluctuations into Cartesian coordinates at the signal redshift. This allowed us to directly obtain contamination power spectra, which are essential to determine the real degree of foreground contamination and to plan ways to clean observational maps.

The C II intensities obtained with these observing cones are shown in Table 7, together with the overall CO intensity from

transitions (2–1) to (6–5) at the same observed frequencies. The results show that CO contamination will dominate observations, especially for low frequencies.

6. INSTRUMENT PARAMETERS

The characteristics of an experiment able to measure the C II intensity and spatial fluctuations will now be briefly discussed.

We propose to use one of two similar setups: the first one (C II–Stage I) is appropriate for optimistic C II models (models with a high C II luminosity density), and the second one (C II–Stage II) has the minimum requirements to ensure a C II power spectra detection in the case of a more pessimistic C II model. The choice of a setup for the C II experiment is mainly dependent on the evolution of the C II luminosity for high redshifts, and so it can be updated when more high-redshift C II observations are available.

The basic experiment proposed here (C II–Stage I) consists in using one stack of independent single-beam, single-polarization spectrometers for each polarization. Each of these spectrometers would contain several bolometers, and each of the stacks would cover a line on the sky via a polarizing grid. The second-stage experimental setup (C II–Stage II) is similar to the first one but covers a much larger area with narrower spectra. The details of the proposed experimental setups are shown in Table 8. The angular resolution of the experiments is (0.5 arcmin)^2 for C II–Stage I and (0.4 arcmin)^2 for C II–Stage II.
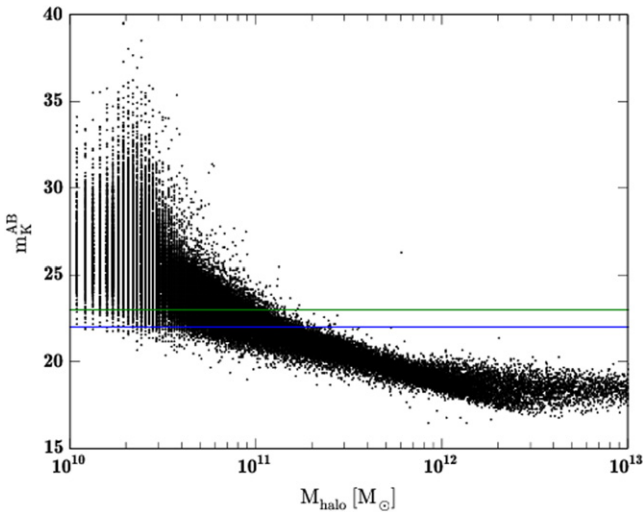
Figure 10. AB magnitude in the K filter vs. halo mass relation at redshift $z = 0.06$. The relation shown has a small evolution with redshift. The horizontal lines show what galaxies are being masked according to the m_K cuts shown in Figure 11.

7. CLEANING CONTAMINATION FROM LOWER-REDSHIFT EMISSION LINES

7.1. Pixel Masking

As was shown in previous sections, the main line contaminants for the planned observations are CO rotation lines from low redshifts. Since the contamination from CO emission lines in the C II power spectra is high, we made CO flux cuts to study which galaxies are dominating the contamination and whether they can be removed from the observational data by masking the pixels with the stronger contaminants.

Given that detecting galaxies with low CO fluxes can be very challenging, we also consider using a CO tracer easier to detect such as the SFR or the relative magnitude in a broadband filter such as the K filter (measured as magnitudes in the AB system in the K filter m_K), which is centered at 2190 nm and covers around 390 nm. The SFR can only be used as a CO tracer in star-forming galaxies. Since there is also an intense CO emission in galaxies powered by AGNs, if we want to use SFR or IR emission as a CO tracer, we should use an additional tracer like observations in the visible band to target the AGNs.

In Figure 10 we can see that galaxies with a high CO flux also have relatively low magnitudes in the K band. Thus, we estimated the m_K cut necessary to reduce the power spectra of CO contamination.

We show in the bottom panels of Figure 11 that for the more optimistic C II models the power spectra of CO contamination can be efficiently reduced by removing from the observational maps contamination by galaxies with CO fluxes in one of the CO rotation lines higher than 5×10^{-22} W m^{-2}, and that this can be done by masking less than 10% of the pixels for an experiment with a setup similar to the C II–Stage II experimental setup. In contrast, the top panels of this figure show that masking in m_K magnitudes is also possible and the necessary masking would require a cut of $m_K = 22$ in order to sufficiently decrease the power spectra of CO contamination predicted for a C II model like $\boldsymbol{m_2}$.

For C II models that yield lower intensities the m_K cut would have to be of $m_K = 23$ or even higher, which would make it impossible to apply the masking technique. The CO masking can be done with cuts in quantities like the CO flux, SFR, IR luminosity, magnitude in a given band, or a combination of probes depending on the CO tracer experiments available. The masking cuts considered in this study are presented in Table 9 following the C II–Stage I or C II–Stage II experimental setups and assuming the Obreschkow CO model. The observational model would require masking CO galaxies until a flux cut of $f_{CO} = 2 \times 10^{-22}$ W m^{-2}, which corresponds to a masking percentage of 10% and 21% for the C II–Stage II and C II–Stage I experimental setups, respectively.

If we are able to measure CO luminosities of some galaxies to a high precision, it will be possible to remove their intensity from each pixel instead of masking the pixel completely. This would reduce the masking percentage. However, the number of galaxies that we can observe with the necessary precision to remove their contamination from observations accurately should be rather small. Also, in order to do this, the intensity of the galaxy would have to be above the "noise" in each of the pixels.

7.2. Cross-correlation with Galaxy Surveys

In this section, we discuss the possibility of using cross correlation as a method to help remove CO foregrounds from C II maps. We start by cross-correlating a CO line with the number density of galaxies.

As is shown in Figure 12, the intensity of CO emission in the CO(5–4) line is strongly correlated with the galaxy number density at the same redshift since they both trace the underlying dark matter density fluctuations.

Here we consider the case that the number density of galaxies is independently measured with a galaxy survey. The number density of galaxies at a redshift $z = 1.4$ can be cross-correlated with an observational intensity map of the CO(5–4) line centered at the same redshift (obtained from the 200–300 GHz observing cone), and the result will be proportional to the intensity fluctuations of the CO(5–4) line even if the intensity map also contains C II and other CO lines. This can be done for several foreground lines and redshifts to probe the degree of contamination by these lines.

7.3. Cross-correlation between Two CO Lines

As can be observed in Table 3, in some cases there are two CO lines originating from the same redshift contaminating the observational maps at two different frequencies. For example, the CO(3–2) and the CO(4–3) emitted at a redshift of $z = 0.6$ will be observed at frequencies of 288.2 and 216.1 GHz, respectively, and so they will contaminate C II intensity maps at redshifts 7.8 and 5.6.

As is shown in Figure 13, the cross-correlation between observational maps with C II plus CO will be stronger than maps with just C II, and so by cross-correlating intensity maps before and after masking, we can confirm whether the cleaning procedure was successful. Also, the existence of contamination from two lines emitted from the same redshift can in principle be implemented in algorithms to help remove the CO contamination, although that task is beyond the objectives of this study.
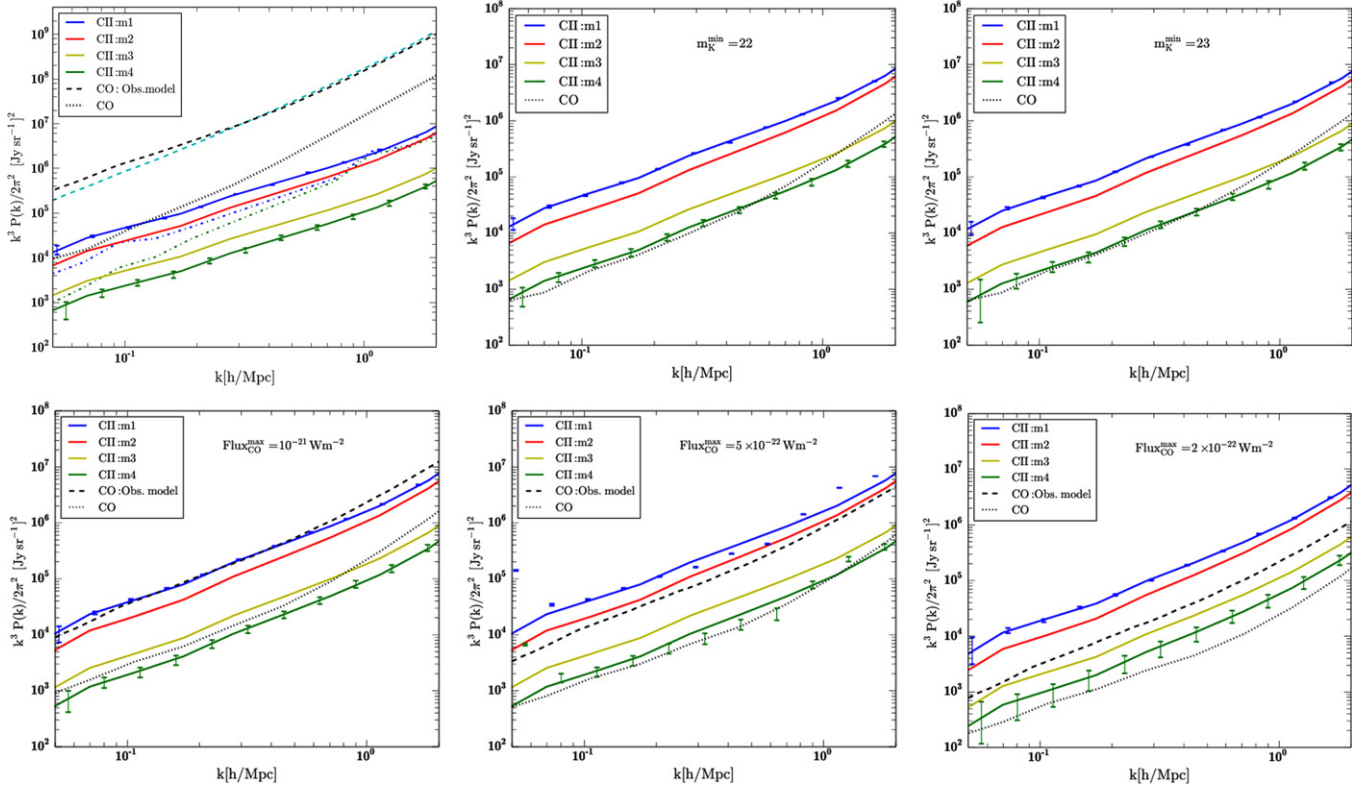
Figure 11. Power spectra of C II emission for four parameterizations of L_{CII} vs. SFR (solid lines) and power spectra of CO contamination (dotted lines) observed in a frequency range of 37 GHz centered at $F_{obs} \approx 250$ GHz. The cyan dot-dashed line corresponds to an upper limit for C II emission from ionized regions. Upper left panel corresponds to the total C II power spectra and CO contamination power spectra. The middle and right upper panels assume only CO sources with AB relative magnitudes in the K band above $m_K = 22$ and $m_K = 23$, respectively. Lower panels assume only CO sources with fluxes below 10^{-21} W m^{-2} (left panel), 5×10^{-22} W m^{-2} (middle panel), and 2×10^{-22} W m^{-2} (right panel). Also shown in the upper left and in the lower panels are dashed lines of the theoretical CO emission, with the same flux cuts, estimated using the CO observationally based model. The error bars in the C II models *m1* and *m4* are based on the experimental setup of the C II–Stage II experiment described in Table 8. Also shown with dot-dashed lines in the top left panel are the errors in the C II models *m1* and *m4* based on the experimental setup of the C II–Stage I experiment described in Table 8.

Table 9
Masking Percentages for an Observation in the
Frequency Range from 200 to 300 GHz

Flux/m_K Cuts	C II-Stage I Masking %	C II-Stage II Masking %
$f_{CO} > 1 \times 10^{-21}$ (W m^{-2})	7.70	1.97
$f_{CO} > 5 \times 10^{-22}$ (W m^{-2})	12.99	3.39
$f_{CO} > 2 \times 10^{-22}$ (W m^{-2})	23.31	6.40
$m_K < 22$	6.23	1.58
$m_K < 23$	13.76	3.60

8. CROSS-CORRELATION BETWEEN THE H I AND C II LINES

Fluctuations in both H I and C II intensity maps are correlated with fluctuations in the underlying density field, and so the spatial distribution of emission in these two lines is correlated. Therefore, the cross-correlation power spectra of the the two lines give a measure of their intensities.

Since C II is emitted from galaxies and H I is emitted from the IGM, these two quantities are mostly negatively correlated at large scales. At small scales the correlation between C II and H I emission should be positive since they are both biased in overdense regions. However, we find no correlation in our
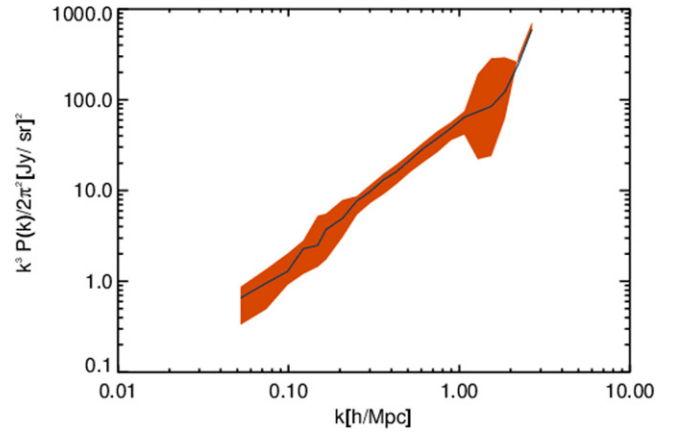

Figure 12. Cross-correlation power spectra between number of galaxies and intensity of the CO(5–4) line at redshift $z = 1.4$ obtained from our simulations. The 1σ uncertainty shown in orange was obtained by cross-correlating these two quantities in different regions of the space.

simulations, which is probably due to the low intensity of 21 cm emission at these scales.

In Figure 14 we show the cross-power spectra between H I emission and two models for C II emission. The error bars shown in this figure were obtained with the H I 21 cm line experiment described in Table 10 and with the C II–Stage II instrument.
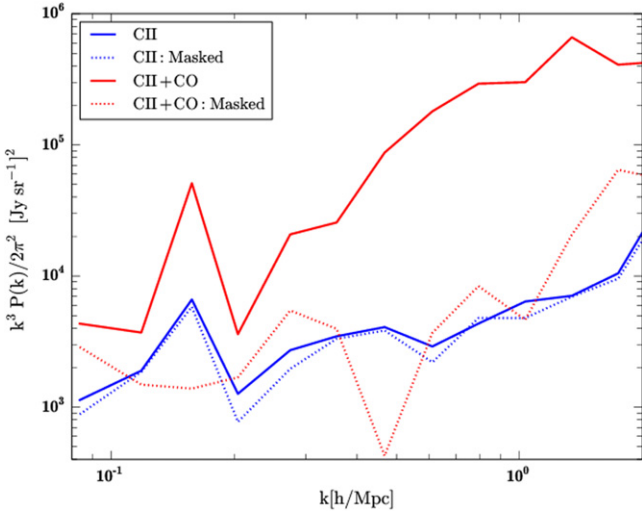
Figure 13. Cross-correlation power spectra between observational maps with 70 Mpc centered at frequencies 288.2 and 216.1 GHz, which correspond to C II emission from redshift 7.8 and 5.6. The blue lines show the cross-correlation obtained from maps with only C II emission. The red lines show the cross-correlation obtained from maps with C II plus CO. Solid lines denote the full signal, while dotted lines denote the signals masked until a CO flux of 2×10^{-22} W m^{-2}. The masking was done assuming the C II–Stage II experimental setup.
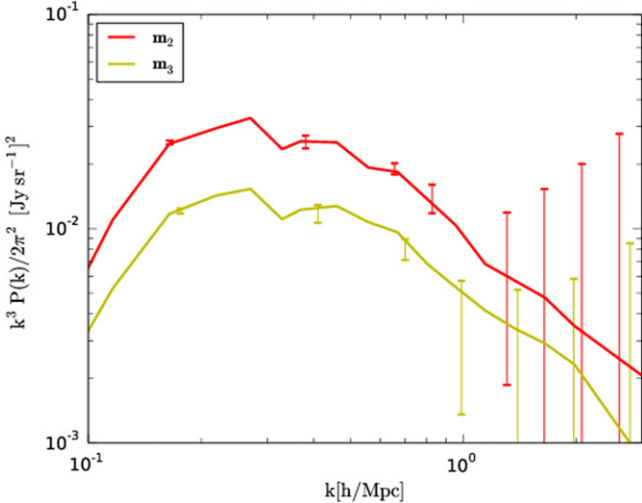

Figure 14. Absolute value of the correlation power spectra between C II emission (models m_2 and m_3) and the neutral hydrogen 21 cm line at redshift $z = 7.0$. The error bars were estimated assuming the C II–Stage II experimental setup. Note that these two lines are negatively correlated at the shown scales.

9. CONCLUSIONS

In this paper we consider the possibility of applying the intensity mapping technique to the C II line at high redshifts in order to probe the EoR and galaxy properties in the early universe. The ionized carbon C II 158 μm line is one of the strongest emission lines in the spectra of star-forming galaxies, and so observing this line is one of the few possible ways to study very distant galaxies. Given the uncertainty in C II emission from high-redshift galaxies, we took into consideration four models for C II emission that cover the uncertainty in the relation between C II emission and SFR. We concluded that intensity mapping of the C II line during the end of the EoR is in the reach of today's technology.

Table 10
Parameters for SKA1-low

Instrument	Value	Unit
Station diameter D_{stat}	35	m
Survey area A_s	6.55	deg^2
FoV per station	6.55	deg^2
Effective area per stat. A_e	355.04	m^2
Frequency resolution $d\nu$	3.9	kHz
Bandwidth ($z = 8 \pm 0.5$) BW	18	MHz
Tot. int. time t_{int}	200	hr
Min. baseline D_{min}	35	m
Max. baseline D_{max}	1	km
Collecting area A_{coll}	307466	m^2
uv$_{min}$	21	…
uv$_{max}$	596	…
T_{sys}	291	K
Effective num. stat.	866	…

The intensity of the C II signal from $z \sim 8.5$ to $z \sim 5.5$ is likely to be between 10^2 and 10^3 Jy sr^{-1}, although higher values would be possible if the SFRD is higher than the current predictions. In the local universe, C II emission from star-forming galaxies is a good probe of their SFR, and so intensity mapping of this line should provide good constraints on the SFRD at high redshifts, even if the constant of proportionality between C II luminosity and SFR evolves with redshift. Although a reasonable dispersion in the C II emission versus SFR relation is expected, in intensity mapping studies, we are averaging the relation over thousands of galaxies in each pixel, so that the total C II emission should be averaged by the SFRD. The C II intensity should be dominated by galaxies with luminosities below the threshold of galaxy surveys, and so even if C II emission in bright galaxies is not a perfect tracer for star formation, it should provide good constraints in the SFRD. The C II line is also dependent on the ISM metallicity, and although C II intensity maps cannot give strong constraints to this quantity, they will provide a lower limit that will be on its own an improvement over current constraints of the gas metallicity at high redshifts. Note that redshift evolution of the metallicity can tell us about the characteristics of Pop II and Pop III stars, which is also particularly important for reionization studies.

Emission from CO rotation lines is going to be the main contaminant in C II observations, and although the CO and C II intensities have a large uncertainty, it is reasonably confirmed that some of the CO signal has to be removed from observations in order to recover the correct C II fluctuations. We estimated the CO intensity using two independent methods, one based on detailed simulations of gas conditions in galaxies and physical relations between CO transitions, and another that uses only observational quantities and observationally based relations between these quantities. Both these methods predict similar CO intensities. The current constraints in CO and C II emission indicate that the CO power spectra will be up to one order of magnitude higher than the C II power spectra. However, we showed that the CO signal can be reduced at least as much, by masking the pixels contaminated by the galaxies with the brighter CO emission.

We described an experiment that is within reach of current technology and is able to measure the C II power spectra with enough resolution that we can mask most of the CO

contamination without erasing the C II signal. In order to identify the most luminous CO galaxies, we propose to use a galaxy survey able to measure CO luminosities or a more modest survey able to detect the galaxies AB magnitudes in the K band, since this is a good tracer of CO luminosity. A galaxy survey able to measure CO luminosities of several transitions until a redshift of at least 2.5 would also provide the first LFs for CO transitions higher than the first CO rotational transition, which would by itself be a valuable contribution to the study of gas conditions of galaxies.

If the CO contamination is too high and the masking technique is not enough to successfully clean the images or in order to confirm whether the contamination was well removed, we can use cross-correlations between different CO lines to estimate the intensity of their contamination. Even in the worst-case scenario where the overall CO emission is a few times higher than what we have considered, we still would be able to remove CO to at least detect the C II signal with the proposed C II–Stage II experimental setup. Moreover, cross-correlation between intensity maps of C II and other lines from the same redshift will not suffer from line contamination.

Finally, the C II line and the 21 cm line are expected to be strongly anticorrelated. By cross-correlating C II and 21 cm maps, we will obtain a statistical estimate of the intensity of these signals independent of most foregrounds, which can be a valuable asset in constraining reionization.

APPENDIX

In this Appendix we summarize the key steps necessary to obtain the continuum foregrounds that will contaminate C II intensity maps in the frequency range 200–300 GHz. This study includes contamination by stellar emission, dust emission, free–free and free–bound emission, and finally two-photon emission.

A.1. Stellar Emission

The stellar luminosity at frequency ν is approximately given by the emissivity of a blackbody (B_ν) integrated over the solid angle and the area of the stellar surface ($4\pi R_*^2$):

$$L_\nu^\star = \pi\, 4\pi\, R_*^2\, B_\nu\left(T_*^{\mathrm{eff}}\right). \tag{23}$$

For estimating the stellar radius (R_*) and for the star effective temperature (T_{eff}) we used the formulas in (Cooray et al. 2012) for Pop II stars and Pop III stars. We calculated separately the emission from Pop II and Pop III stars assuming that the Pop III

stellar population evolution could be described using the error function. The error function is given by

$$fp(z') = \frac{1}{2}\left[1 + \mathrm{erf}\left(\frac{z - zt}{\sigma_{\mathrm{p}}}\right)\right], \tag{24}$$

where we imposed that the Pop III population ended at $z = 6$, that Pop III stars are the dominant population for $z_t \geqslant 10$, and that the Pop III transition width is $\sigma_{\mathrm{P}} = 0.5$. A discussion for the choice of these values can be found at Fernandez & Zaroubi (2013).

The observed stellar luminosity density is the sum of the luminosity density of Pop II stars (l^{POPII}) and of Pop III stars (l^{POPIII}), given respectively by

$$l^{\mathrm{POP_{II}}}(\nu, z) = \int_z^{z_{\mathrm{max}}} \int_{M_*^{\mathrm{min}}}^{M^{\mathrm{cut}(z,z')_*}} K(z') M_*^{-2.35} L_\nu^\star$$
$$\times\, dM_*'\, \frac{dt}{dz'}\, dz', \tag{25}$$

and

$$l^{\mathrm{POP_{III}}}(\nu, z) = \int_z^{z_{\mathrm{max}}} \int_{M_*^{\mathrm{min}}}^{M_*^{\mathrm{cut}(z')}} K(z') M_*^{-1}\left(1 + \frac{M_*}{M_*^c}\right)^{-1.35}$$
$$\times\, L_\nu^*\, dM_*\, \frac{dt}{dz'}\, dz'. \tag{26}$$

We integrated in stellar mass using a Salpeter (1955) initial mass function (IMF) with a mass range from 0.1 to 100 $M_\odot$ for Pop II stars and a Larson (1998) IMF with a mass range from 0.1 to 500 $M_\odot$ and $M_*^c = 250$ M$_\odot$ for Pop III stars. In Equations (25) and (26), $M^{\mathrm{cut}}(z, z')$ corresponds to the maximum stellar mass of a star created at redshift z' that is still alive, and $K(z')$ is the normalization of the mass function in units of [Mpc^{-3} s^{-1}], so that the total stellar mass coincides with the value that can be obtained with the SFRD Ψ in units of $M_\odot$ Mpc^{-3} s^{-1}. For Pop II and Pop III stars $K(z')$ is given, respectively, by

$$K(z') = \frac{\Psi(z') fp(z')}{\int_{M_*^{\mathrm{min}}}^{M_*^{\mathrm{max}}} M_*^{-2.35}\, M_*\, dM_*'} \tag{27}$$

and

$$K(z') = \frac{\Psi(z')[1 - fp(z')]}{\int_{M_*^{\mathrm{min}}}^{M_*^{\mathrm{max}}} M_*^{-1}\left(1 + \frac{M_*}{M_*^c}\right)^{-1.35} M_*\, dM_*'}. \tag{28}$$

The stellar emission contamination to the observed frequency ν_o is given by

$$I_{\nu_o} = \int_{z=0}^{z_{\mathrm{max}}} y(z') \frac{l^{\mathrm{POP_{II}}}(\nu, z') + l^{\mathrm{POP_{III}}}(\nu, z')}{4\pi(1 + z')^2} dz', \tag{29}$$

where ν is the emitted frequency, which is related to the observed frequency by $\nu = \nu_o(1 + z)$. The resulting intensity in the 200–300 GHz frequency range is $I_\nu \approx 2.5 \times 10^{-4}$ Jy sr^{-1}.

A.2. Dust Emission

UV emission from stars between 13.6 and 6 eV is absorbed by the dust in the galaxy and is re-emitted as continuum IR radiation. The dust spectral emission is the result of emission by dust particles with different sizes emitting at a temperature proportional to the particle size. Each particle emits approximately as a blackbody, and so the overall emission spectra are well described by blackbody spectra at temperature T_d, modified by the emissivity function $\epsilon_\nu \propto \nu^\beta$ in order to account for the different dust temperatures. Using the data from the Herschel-Astrophysical Terahertz Large Area Survey and from the Sloan Digital Sky Survey, Amblard et al. (2010) estimated that $\beta \approx 1.5$ and that the dust temperature as a function of the IR luminosity can be approximated by

$$T_d = T_0 + \alpha \, \log\big(L_{\mathrm{IR}} / L_\odot\big), \quad (30)$$

with $T_0 = -20.5$ K and $\alpha = 4.4$. The data set used for this fit contains galaxies with $L_{\mathrm{FIR}} > 10^8 \, L_\odot$ and is not accurate for lower-luminosity galaxies. So for lower-luminosity galaxies we assumed that $T_d = T_d(L_{\mathrm{IR}} = 10^8 \, L_\odot) \approx 10$ K. We set the amplitude of the dust emission (A_{dust}) by imposing that

$$A_{\mathrm{dust}} = \frac{L_{\mathrm{FIR}}(40 - 120 \, \mu m)}{\displaystyle\int_{40\,\mu m}^{120\,\mu m} \nu_{\mathrm{e}}^\beta \, \frac{\nu_{\mathrm{e}}^3}{e^{(h\nu_{\mathrm{e}}/kT_d)} - 1}}, \quad (31)$$

where L_{IR} and L_{FIR} can be obtained from the galaxy mass using Equations (5), (4), and (8). The observed intensity originated from dust emission will therefore be:

$$
\begin{aligned}
I_\nu = \int_{z_{\min}}^{z_{\max}} \int_{M_{\min}}^{M_{\max}} \frac{dn}{dm} \frac{A_{\mathrm{dust}} \, \nu_{\mathrm{e}}^\beta \, \dfrac{\nu_{\mathrm{e}}^3}{e^{(h\nu_{\mathrm{e}}/kT_d)} - 1}}{4 \, \pi \, D_{\mathrm{L}}^2} \\
\times D_{\mathrm{A}}^2 \, y(\nu_{\mathrm{e}}) dM \, dz
\end{aligned}
\quad (32)
$$

where $\nu_{\mathrm{e}} = \nu \, (1 + z)$. The resulting intensity is of the order of 10^{-5} Jy sr^{-1}. The contamination from dust emission will be orders of magnitude above the C II intensity in the 200–300 GHz observing frequency range. This continuum contamination can be removed from observational maps due to its smooth evolution with frequency.

A.3. Free–Free, Free–Bound, and Two-photon Emission

Free electrons scatter off ions without being captured, giving origin to free–free continuum emission. If during this interaction the electrons are captured by the ions, then there is emission of free–bound radiation. In these same ionized regions there occur hydrogen recombinations that originate Lyα photons or two-photon emission. Following the approach of Fernandez & Komatsu (2006), the free–free, free–bound, and two-photon continuum luminosities can be obtained using

$$L_\nu(M, z) = V_{\mathrm{sphere}}(M, z)\varepsilon_\nu \quad (33)$$

where V_{sphere} is the volume of the Strömgren sphere (the emitting volume), which can be roughly estimated using the ratio between the number of ionizing photons emitted by a halo and the number density of recombinations in the ionized volume:

$$V_{\mathrm{sphere}}(M, z) = \frac{Q_{\mathrm{ion}} \, \psi(M, z)\big(1 - f_{\mathrm{esc}}\big)}{n_{\mathrm{e}} \, n_{\mathrm{p}} \, \alpha_{\mathrm{B}}}, \quad (34)$$

where ε_ν is the total volume emissivity of free–free, free–bound, and two-photon emission, Q_{ion} is the average number of ionizing photons per solar mass in star formation, n_{e} is the number density of free electrons, n_{p} is the number density of protons (ionized atoms), and α_{B} is the case B recombination coefficient (taken from Furlanetto et al. 2006), given by

$$\alpha_{\mathrm{B}} \approx 2.6 \times 10^{-13} \left(T_{\mathrm{K}}/10^4 \, \mathrm{K}\right)^{-0.7} (1 + z)^3 \, \mathrm{cm}^3 \, \mathrm{s}^{-1}, \quad (35)$$

and f_{esc} is the ionizing photon escape fraction. In our calculations we used the redshift- and halo-mass-dependent escape fraction of ionizing radiation from Razoumov & Sommer-Larsen (2010), and we used $Q_{\mathrm{ion}} = 5.38 \times 10^{60} \, M_\odot^{-1}$, appropriate for Pop II stars (Silva et al. 2013).

The volume emissivity from free–free and free–bound emission estimated by (Dopita & Sutherland 2003) is given by

$$\varepsilon_\nu^{\mathrm{free}} = 4\pi \, n_{\mathrm{e}} \, n_{\mathrm{p}} \, \gamma_c \, \frac{e^{-h\nu/kT_{\mathrm{K}}}}{T_{\mathrm{K}}^{1/2}} \, \mathrm{J} \, \mathrm{cm}^{-3} \, \mathrm{s}^{-1} \, \mathrm{Hz}^{-1}, \quad (36)$$

where γ_c is the continuum emission coefficient for free–free and free–bound emission given in SI units by

$$\gamma_c = 5.44 \times 10^{-46}\left[\bar{g}_{\mathrm{ff}} + \Sigma_{n=n'}^\infty \frac{x_n e^{x_n}}{n} g_{\mathrm{fb}}(n)\right], \quad (37)$$

where $x_n = \mathrm{Ry} \big/(k_{\mathrm{B}} \, T_{\mathrm{K}} \, n^2)$ (n is the level to which the electron recombines, and $\mathrm{Ry} = 13.6$ eV is the Rydberg unit of energy), and $\bar{g}_{\mathrm{ff}} \approx 1.1$–1.2 and $g_{\mathrm{fb}}(n) \approx 1.05$–1.09 are the thermally averaged Gaunt factors for free–free and free–bound emission, respectively (values from Karzas & Latter 1961). The initial level n' is determined by the emitted photon frequency and satisfies the condition $c \, R_\infty \big/ n'^2 < \nu < c \, R_\infty \big/(n' - 1)^2$, where $R_\infty = 1.1 \times 10^7 \, \mathrm{m}^{-1}$ is the Rydberg constant. We then obtained the free–free plus free–bound luminosity formula, given by

$$
\begin{aligned}
L_\nu^{\mathrm{free}}(M, z) = 3.68 \times 10^{16} \, \alpha_{\mathrm{B}}^{-1}\left(T_{\mathrm{K}}, z\right)\left[\frac{Q_{\mathrm{ion}}}{5.38 \times 10^{60}}\right] \\
\times \left[1.15 + \Sigma_{n=n'}^\infty \frac{x_n \, e^{x_n}}{n} 1.07\right] \\
\times \frac{e^{-h\nu/k_{\mathrm{B}}T_{\mathrm{K}}}}{T_{\mathrm{K}}^{1/2}} \psi(M, z).
\end{aligned}
\quad (38)
$$

The two-photon luminosity is given by

$$L_\nu^{2\gamma}(M) = \frac{2 \, h\nu}{\nu_{\mathrm{Ly}\alpha}} \left(1 - f_{\mathrm{Ly}\alpha}\right)P(\nu/\nu_{\mathrm{Ly}\alpha})Q_{\mathrm{ion}} \psi(M, z), \quad (39)$$

where $P(y)dy$ is the normalized probability that in a two-photon decay one of them is the range $dy = d\nu/\nu_{\mathrm{Ly}\alpha}$ and $1 - f_{\mathrm{Ly}\alpha} \approx 1/3$ is the probability of two-photon emission during a hydrogen $n = 2 \rightarrow 1$ transition. The probability of two-photon decay was fitted by Fernandez & Komatsu (2006)

using Table 4 of Brown & Mathews ([1970](#)) as

$$P(y) = 1.307 \ - \ 2.627 \, (y \ - \ 0.5)^2$$
$$+ \ 2.563 \, (y - 0.5)^4 \ - \ 51.69 \, (y - 0.5)^6. \qquad (40)$$

The intensity from nebula continuum emission is given by

$$I_{\mathrm{cont}}(\nu) = \int_{z=0}^{z_{\max}} \ dz \ \frac{L_{\mathrm{cont}}(\nu_e, z)}{4\pi \, D_L^2} \, y \, D_A^2, \qquad (41)$$

where $L_{\mathrm{cont}} = L_\nu^{2\gamma} + L_\nu^{\mathrm{free}}$.

Assuming a gas temperature of $(1-4) \times 10^4$ K, we estimated the intensity of nebula continuum emission in the frequency range 200–300 GHz to be $I_{\mathrm{cont}}(\nu) = I_{\mathrm{free}} + I_{2\gamma} \approx (0.9\text{–}1.3) \times 10^1 \, \mathrm{Jy \ sr^{-1}} + (1.8\text{–}7.2) \times 10^{-13} \, \mathrm{Jy \ sr^{-1}} = (0.9\text{–}1.2) \times 10^1 \, \mathrm{Jy \ sr^{-1}}$. Therefore, the nebula continuum emission is dominated by dust emission and is above the expected C II signal, and so it can easily be removed by taking advantage of the smooth evolution of this foreground with frequency.

REFERENCES

Aannestad, P. A., & Emery, R. J. 2003, A&A, 406, 155
Amblard, A., Cooray, A., Serra, P., et al. 2010, A&A, 518, L9
Aravena, M., Carilli, C. L., Salvato, M., et al. 2012, MNRAS, 426, 258
Boselli, A., Gavazzi, G., Lequeux, J., & Pierini, D. 2002, A&A, 385, 454
Bouwens, R. J., Illingworth, G. D., Oesch, P. A., et al. 2012, ApJ, 754, 83
Boylan-Kolchin, M., Springel, V., White, S. D. M., Jenkins, A., & Lemson, G. 2009, MNRAS, 398, 1150
Brauher, J. R., Dale, D. A., & Helou, G. 2008, ApJS, 178, 280
Brown, R. L., & Mathews, W. G. 1970, ApJ, 160, 939
Capak, P. L., Carilli, C., Jones, G., et al. 2015, arXiv
Cardiel, N., Elbaz, D., Schiavon, R. P., et al. 2003, ApJ, 584, 76
Carilli, C. L. 2011, ApJL, 730, L30
Carilli, C. L., & Walter, F. 2013, ARA&A, 51, 105
Carral, P., Hollenbach, D. J., Lord, S. D., et al. 1994, ApJ, 423, 223
Chapman, E., Abdalla, F. B., Harker, G., et al. 2012, MNRAS, 423, 2518
Cooray, A., Gong, Y., Smidt, J., & Santos, M. G. 2012, ApJ, 756, 92
Daddi, E., Bournaud, F., Walter, F., et al. 2010, ApJ, 713, 686
Daddi, E., Dannerbauer, H., Liu, D., et al. 2015, A&A, 577, A46
De Looze, I., Baes, M., Bendo, G. J., Cortese, L., & Fritz, J. 2011, MNRAS, 416, 2712
De Looze, I., Cormier, D., Lebouteiller, V., et al. 2014, A&A, 568, A62
De Lucia, G., & Blaizot, J. 2007, MNRAS, 375, 2
Dopita, M. A., & Sutherland, R. S. 2003, Astrophysics of the Diffuse Universe (Berlin: Springer)
Ferkinhoff, C., Brisbin, D., Nikola, T., et al. 2011, ApJL, 740, L29
Fernandez, E. R., & Komatsu, E. 2006, ApJ, 646, 703
Fernandez, E. R., & Zaroubi, S. 2013, MNRAS, 433, 2047
Furlanetto, S. R., Oh, S. P., & Briggs, F. H. 2006, PhR, 433, 181
Gong, Y., Cooray, A., Silva, M., et al. 2012, ApJ, 745, 49
Gong, Y., Silva, M., Cooray, A., & Santos, M. G. 2014, ApJ, 785, 72
González-López, J., Riechers, D. A., Decarli, R., et al. 2014, ApJ, 784, 99
Graciá-Carpio, J., Sturm, E., Hailey-Dunsheath, S., et al. 2011, ApJL, 728, L7
Guo, Q., White, S., Boylan-Kolchin, M., et al. 2011, MNRAS, 413, 101
Hollenbach, D. J., & Tielens, A. G. G. M. 1997, ARA&A, 35, 179
Kaneda, H., Nakagawa, T., Ghosh, S. K., et al. 2013, A&A, 556, A92
Kanekar, N., Wagg, J., Ram Chary, R., & Carilli, C. L. 2013, ApJL, 771, L20
Karzas, W. J., & Latter, R. 1961, ApJS, 6, 167
Kaufman, M. J., Wolfire, M. G., Hollenbach, D. J., & Luhman, M. L. 1999, ApJ, 527, 795
Kennicutt, R. C., Jr. 1998, ApJ, 498, 541
Kistler, M. D., Yuksel, H., & Hopkins, A. M. 2013, arXiv
Lagos, C. D. P., Baugh, C. M., Lacey, C. G., et al. 2011, MNRAS, 418, 1649
Lagos, C. D. P., Bayet, E., Baugh, C. M., et al. 2012, MNRAS, 426, 2142
Larson, R. B. 1998, MNRAS, 301, 569
Lebouteiller, V., Cormier, D., Madden, S. C., et al. 2012, A&A, 548, A91
Malhotra, S., Kaufman, M. J., Hollenbach, D., et al. 2001, ApJ, 561, 766
Mellema, G., Koopmans, L. V. E., Abdalla, F. A., et al. 2013, ExA, 36, 235
Obreschkow, D., Heywood, I., Klöckner, H.-R., & Rawlings, S. 2009a, ApJ, 702, 1321
Obreschkow, D., Klöckner, H.-R., Heywood, I., Levrier, F., & Rawlings, S. 2009b, ApJ, 703, 1890
Ota, K., Walter, F., Ohta, K., et al. 2014, ApJ, 792, 34
Paciga, G., Chang, T.-C., Gupta, Y., et al. 2011, MNRAS, 413, 1174
Parsons, A. R., Backer, D. C., Foster, G. S., et al. 2010, AJ, 139, 1468
Pineda, J. L., Langer, W. D., Velusamy, T., & Goldsmith, P. F. 2013, A&A, 554, A103
Razoumov, A. O., & Sommer-Larsen, J. 2010, ApJ, 710, 1239
Rigopoulou, D., Hopwood, R., Magdis, G. E., et al. 2014, ApJL, 781, L15
Rigopoulou, D., Hurley, P. D., Swinyard, B. M., et al. 2013, MNRAS, 434, 2051
Robertson, B. E., & Ellis, R. S. 2012, ApJ, 744, 95
Rottgering, H. J. A., Braun, R., Barthel, P. D., et al. 2006, in Proc. of Cosmology, Galaxy Formation and Astroparticle Physics on the Pathway to the SKA, ed. H.-R. Klöckner, et al. (Dwingeloo: ASTRON), 169
Salpeter, E. E. 1955, ApJ, 121, 161
Santos, M. G., Cooray, A., & Knox, L. 2005, ApJ, 625, 575
Santos, M. G., Ferramacho, L., Silva, M. B., Amblard, A., & Cooray, A. 2010, MNRAS, 406, 2421
Sargent, M. T., Béthermin, M., Daddi, E., & Elbaz, D. 2012, ApJL, 747, L31
Sargent, M. T., Daddi, E., Béthermin, M., et al. 2013, ApJ, 793, 19
Sargsyan, L., Lebouteiller, V., Weedman, D., et al. 2012, ApJ, 755, 171
Shaver, P. A., Windhorst, R. A., Madau, P., & de Bruyn, A. G. 1999, A&A, 345, 380
Sheth, R. K., & Tormen, G. 1999, MNRAS, 308, 119
Silva, M., Santos, M. G., Gong, Y., & Cooray, A. 2013, ApJ, 763, 132
Soifer, B. T., Boehmer, L., Neugebauer, G., & Sanders, D. B. 1989, AJ, 98, 766
Springel, V., White, S. D. M., Jenkins, A., et al. 2005, Natur, 435, 629
Stacey, G. J., Hailey-Dunsheath, S., Ferkinhoff, C., et al. 2010, ApJ, 724, 957
Stacey, G. J., Swain, M. R., Bradford, C. M., et al. 1999, in ESA Special Publication 427, The Universe as Seen by ISO, ed. P. Cox & M. Kessler (Noordwijk: ESA), 973
Tacconi, L. J., Genzel, R., Neri, R., et al. 2010, Natur, 463, 781
Tingay, S. J., Goeke, R., Bowman, J. D., et al. 2013, PASA, 30, 7
Venkatesan, A. 2000, ApJ, 537, 55
Wang, R., Wagg, J., Carilli, C. L., et al. 2013, ApJ, 773, 44
Zhao, Y., Lu, N., Xu, C. K., et al. 2013, ApJL, 765, L13